


# Engineered macrophage nanoparticles enhance microwave ablation efficacy in osteosarcoma via targeting the CD47-SIRP $\alpha$ Axis: A novel Biomimetic immunotherapeutic approach

Xiongfai Ji<sup>a,1</sup>, Xin Qian<sup>b,1</sup>, Guowen Luo<sup>a,c,d,1</sup>, Wenjie Yang<sup>a,c,d</sup>, Wenhan Huang<sup>a,c,d</sup>, Zehua Lei<sup>a,d</sup>, Jiaqi Zhou<sup>a,c,d</sup>, Guoqing Zhong<sup>a,c,d</sup>, Jielong Zhou<sup>a,c,d</sup>, Nan Liu<sup>a</sup>, Limin Ma<sup>a,c,d</sup>, Mei Li<sup>a,c,d,\*</sup>, Xiangmei Liu<sup>e,\*\*</sup>, Shuilin Wu<sup>f,\*\*\*</sup>, Yu Zhang<sup>a,c,d,\*\*\*\*</sup> 

<sup>a</sup> Department of Orthopedics, Guangdong Provincial People's Hospital, Guangdong Academy of Medical Sciences, Southern Medical University, 510080, Guangzhou, China

<sup>b</sup> Beijing Tsinghua Changgung Hospital, School of Clinical Medicine, Tsinghua University, No.168 Litang Road, Changping District, 100000, Beijing, China

<sup>c</sup> Guang Dong Engineering Technology Research Center of Functional, Repair of Bone Defects and Biomaterials, 510080, Guangzhou, China

<sup>d</sup> Medical Research Center, Department of Orthopedics, Guangdong Provincial People's Hospital, Guangdong Academy of Medical Sciences, Southern Medical University, 510080, Guangzhou, China

<sup>e</sup> School of Health Science & Biomedical Engineering, Hebei University of Technology, Xiping Avenue 5340, 300401, Tianjin, China

<sup>f</sup> School of Materials Science & Engineering, Peking University, Yi-He-Yuan Road 5, 100871, Beijing, China

## ARTICLE INFO

### Keywords:

Osteosarcoma  
Nano prussian blue  
Macrophage cell membrane  
Microwave responsive

## ABSTRACT

Osteosarcoma (OS) is a lethal bone tumor that primarily affects adolescents. OS is characterized by a high incidence of recurrence following surgical intervention, which is attributed to the presence of residual microscopic disease. Tumor-associated macrophages, which dominate the tumor microenvironment, often suppress immune responses and facilitate tumor progression and recurrence. This study developed an innovative nano-therapeutic approach by utilizing genetically engineered macrophage membranes with M1 polarization, stably overexpressing signal regulatory protein alpha (SIRP $\alpha$ ), to encapsulate microwave-responsive nano-Prussian blue (SIRP $\alpha$ -M@nanoPB) nanoparticles. These nanoparticles induce tumor cell death selectively through hyperthermia and microwave dynamic effects upon targeted microwave irradiation. It is of critical importance to note that the enhancement of SIRP $\alpha$  on the nanoparticle surface actively targets and binds CD47 of tumor cells, thereby disrupting the "don't-eat-me" signal and effectively countering the immunosuppressive tumor environment. This action restores macrophage phagocytosis with M1 polarization, triggering potent immune responses. Our strategy holds considerable promise when it comes to improving the efficacy of microwave ablation through immune modulation, while reducing thermal damage to adjacent normal tissue and minimizing the risk of tumor recurrence. Thus, it offers a significant advancement in microwave therapies for patients with OS.

## 1. Introduction

Osteosarcoma (OS), a prevalent bone tumor in young adolescents,

originates from the mesenchymal tissue with osteoblastic differentiation. Typically, OS develops in the metaphysis of long bones, such as the tibial plateau and femoral condyle [1]. Treatment strategies for OS,

\* Corresponding author. Department of Orthopedics, Guangdong Provincial People's Hospital, Guangdong Academy of Medical Sciences, Southern Medical University, 510080, Guangzhou, China.

\*\* Corresponding author.

\*\*\* Corresponding author.

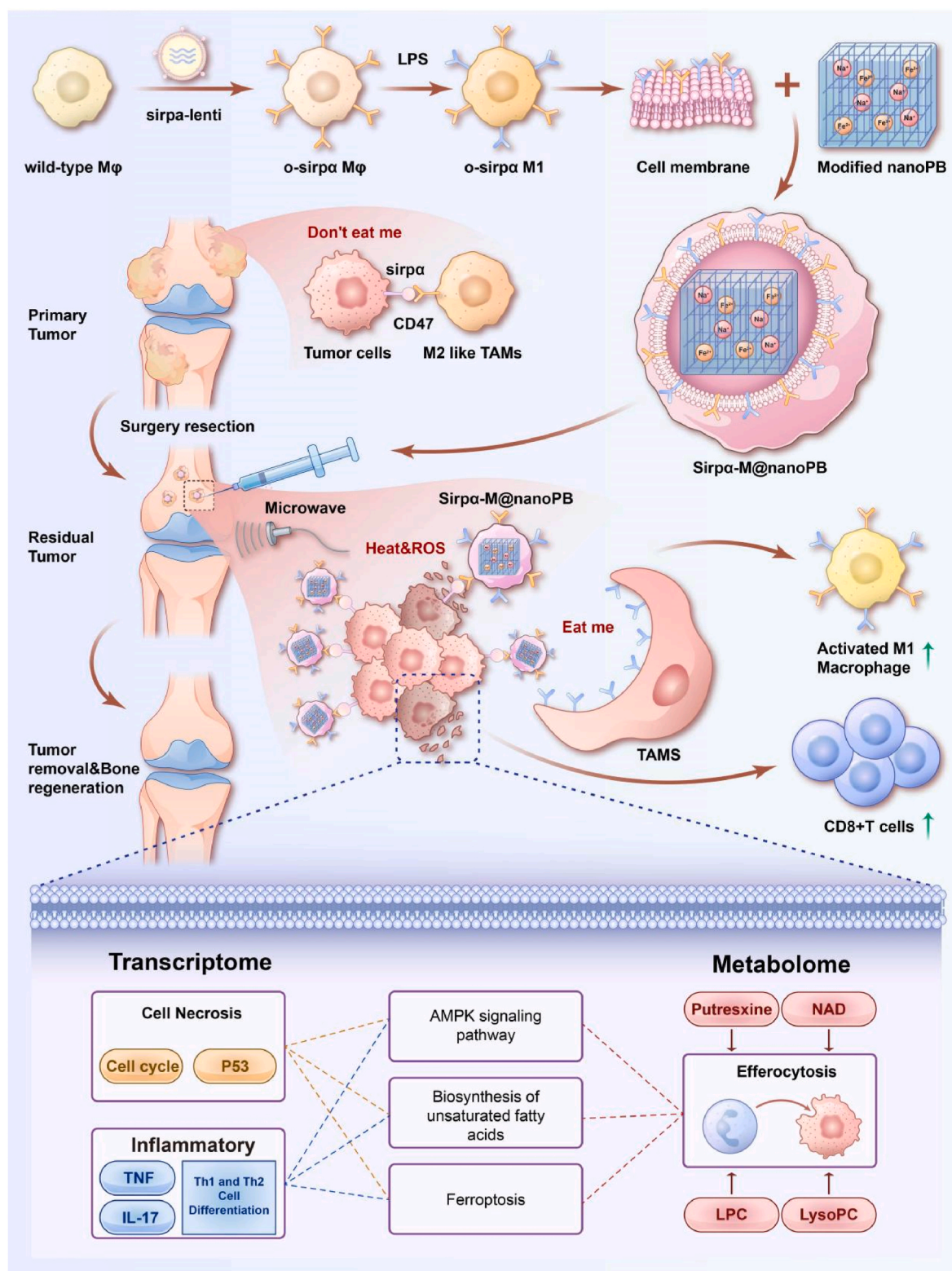
\*\*\*\* Corresponding author. Department of Orthopedics, Guangdong Provincial People's Hospital, Guangdong Academy of Medical Sciences, Southern Medical University, 510080, Guangzhou, China.

E-mail addresses: [limei@gdph.org.cn](mailto:limei@gdph.org.cn) (M. Li), [liuxiangmei1978@163.com](mailto:liuxiangmei1978@163.com) (X. Liu), [slwu@pku.edu.cn](mailto:slwu@pku.edu.cn) (S. Wu), [Zhangyu@gdph.org.cn](mailto:Zhangyu@gdph.org.cn) (Y. Zhang).

<sup>1</sup> These authors contributed equally to this work.

including complete resection combined with standard chemotherapy, targeted therapy, immunotherapy, and emerging therapies, have considerably improved the 5-year survival rate [2]. Despite notable progress in treatment approaches, certain patients with OS continue to experience a poor prognosis, mainly due to metastasis and local recurrence [3]. Based on clinical data, the prognosis for patients with

metastatic OS is discouraging, with a survival rate of <5 years [4]. Furthermore, >80 % of patients develop lung metastasis, and invisible metastases occur at their initial presentation [5,6]. Therefore, developing effective strategies to overcome the invisible residual microtumor and prevent tumor metastasis is crucial for improving patient survival rates [7]. Consequently, practical approaches are needed to tackle the



**Schema 1.** Engineered Macrophage Nanoparticles Enhance Microwave Ablation Efficacy in Osteosarcoma via Targeting the CD47-SIRPα Axis: A Novel Immunotherapeutic Approach.

challenges posed by these microtumors that may persist even after primary treatment. Adjuvant therapy, such as chemotherapy, radiation therapy, or targeted therapy, can be used to eliminate any remaining cancer cells [8]. Moreover, targeting the tumor microenvironment (TME), which includes the surrounding tissues and cells that support tumor growth, is essential. This targeting can be achieved through interventions such as immunotherapy or anti-angiogenic therapy [9]. By adopting a comprehensive approach, it is possible to successfully overcome residual microtumors and prevent tumor metastasis, ultimately improving patient survival (see Scheme 1).

Microwave ablation is an electromagnetic wave ablation technique with frequencies ranging from 900 to 2450 MHz. It is characterised by rapid heat generation due to dipole heating and ion heating caused by charged ions [10]. It is employed in the treatment of diseases such as lung cancer [11] and liver cancer [12], and its side effects are negligible during local treatment. The application of microwave ablation therapy in osteosarcoma has been enhanced by the improvement in prognosis with neoadjuvant chemotherapy, with both physicians and patients aiming to enhance the quality of life for patients, making limb salvage treatment a trend [13,14]. Compared to joint replacement, microwave ablation therapy has the advantage of reducing postoperative infections, long-term loosening, and revisions, which are complications that occur after joint replacement [15]. However, the therapeutic efficacy of microwave ablation is contingent on several factors, including the operational procedure, the intraoperative ablation effects, the operator's personal experience, and the tumor morphology, thereby limiting its application [16]. However, the employment of microwave-responsive nanomaterials offers a potential solution by virtue of their unique physicochemical properties, which enable local heating and targeted treatment of tumour tissues [17,18]. The utilisation of these materials has the potential to enhance the efficacy of microwave ablation, reduce thermal damage to surrounding normal tissues, and decrease the recurrence rate of tumors.

The TME-associated immune suppression is considered crucial in to be a critical determinant of tumor recurrence and metastasis [19]. In the TME of OS, the interaction of tumor-associated macrophages (TAMs) with other cells is involved in the disease progression [20]. Tumor cells often manipulate macrophages and create an immunosuppressive, pro-tumor microenvironment as part of their survival strategies [21]. In addition, the presence of M2-type macrophages inhibits T-cell proliferation and prevents the production of pro-inflammatory cytokines, thereby exacerbating the observed immunosuppression [22]. Immune suppression can also be achieved by manipulating immune checkpoints, such as the CD47-signal regulatory protein alpha (SIRPα) pair in solid tumors [23]. In the context of OS, CD47 (which is expressed on cancer cells [24]) interacts with SIRPα on immune cells, and subsequent signaling inhibits the activity of immune cells, preventing them from attacking the tumor [25]. This mechanism of immune evasion allows the tumor to evade immune detection. It also promotes its growth and spread by initiating the "don't-eat-me" signaling pathway, thereby suppressing the immune response within the TME [26]. Researchers have been actively investigating the ways to target the CD47-SIRPα interaction to overcome immune suppression and enhance anti-tumor immune responses [27,28].

Cell membrane-coated nanoparticles have emerged as a promising area of research in cancer treatment [29]. These nanoparticles are designed by coating synthetic nanoparticles with the cell membranes derived from various cells, such as immune or cancer cells [30]. This approach allows for the replication of the natural properties and functions of the cell membrane, enabling the nanoparticles to mimic the behavior of the original cells. For cancer treatment, cell membrane-coated nanoparticles have shown considerable potential in enhancing drug delivery, improving the immune system recognition of cancer cells, and reducing side effects [31]. The nanoparticles can effectively target tumors, evade immune detection, and specifically release therapeutic payloads at the tumor site [32]. The use of cell membrane-coated

nanoparticles represents a novel and exciting strategy in cancer treatment, with the potential to revolutionize the field and improve patient outcomes.

Herein, inspired by the strategy of CD47-SIRPα blockade and macrophage coating to improve selectivity and efficacy against tumors, a SIRPα-overexpressed cell membrane with M1 polarization has been designed to coat microwave-responsive Prussian blue (PB) nanoparticles (SIRPα-M@nanoPB). This innovative design allows for highly targeted delivery to OS cells and exhibits a synergistic effect in the treatment of OS through multiple mechanisms, including microwave hyperthermia, microwave dynamic effect, and immune regulation. The engineered macrophage cell membrane can actively target tumor cells and competitively bind to block the CD47-SIRPα checkpoint to break immune suppression. The microwave-responsive nature of selected modified nanoPB enables precise and controlled heating of the tumor, which causes localized hyperthermia that can effectively kill OS cells. Through *in vivo* and *in vitro* experiments, we explored the highly targeted, anti-tumor and immunoregulatory mechanisms of the SIRPα-M@nanoPB and validated their effectiveness in a residual OS animal model. This innovative approach holds considerable promise for treating OS, offering a comprehensive and targeted therapeutic strategy that harnesses the power of microwave technology and immune modulation.

## 2. Results and discussion

### 2.1. Design and fabrication of SIRPα-M@nanoPB

To fabricate the SIRPα-overexpressed macrophage membrane, genetically engineered RAW264.7 cells were designed first (Fig. S1 and S2A). As shown in Fig. S1, infection with lentivirus (referred to as LV) and selection with puromycin successfully overexpressed recombinant SIRPα protein on the cell membrane as confirmed via RT-qPCR and western blotting. To validate that SIRPα-overexpressing RAW264.7 macrophages (SIRPα-RAW) can still undergo M1 polarization, RT-qPCR was used to evaluate the expression of genes related to M1 gene expression (Fig. S2B–J). The findings indicate that both the SIRPα-overexpressing (SIRPα-RAW) and the wild-type (W-RAW) groups exhibited significantly increased gene expression of iNOS and TNF-α when stimulated by LPS (SIRPα-RAW to SIRPα-RAW@M1, W-RAW to W-RAW@M1). Similarly, western blotting analysis confirmed that SIRPα-RAW can undergo M1 polarization. The protein levels of IL-1β, iNOS, and TNF-α were consistently higher in the SIRPα-RAW@M1 group compared with that in other groups. Furthermore, we evaluated the influence of M1 polarization on the SIRPα expression in RAW264.7 cells and SIRPα-RAW cells. As illustrated in Figure S2E, the expression levels of SIRPα mRNA in cells from each group following M1 polarization were examined. A comparison of the W-RAW@M1 group with the W-RAW group, and the SIRPα-RAW@M1 group with the SIRPα-RAW group, revealed that following M1 polarization, SIRPα mRNA expression levels exhibited a downward trend in both cell groups. It is noteworthy that the sirpa mRNA expression level in the SIRPα-RAW@M1 group was significantly higher than that in the W-RAW@M1 group. Furthermore, Fig. S2J demonstrated the expression level of the sirpa protein in cells of each group following M1 polarization. The comparison between the W-RAW@M1 group and the W-RAW group, and the SIRPα-RAW@M1 group and the SIRPα-RAW group demonstrated that the expression level of SIRPα protein in the two cells also decreased after M1 polarization. In terms of protein expression, the SIRPα protein expression level of the SIRPα-RAW@M1 group was still significantly higher than that of the W-RAW@M1 group. These results indicated that, although the expression level of SIRPα was generally decreased during the polarization of macrophages M1, the expression level of SIRPα-RAW@M1 cells was still higher than that of W-RAW@M1 cells [33]. These findings lend further support to the potential of SIRPα-RAW@M1 as a cell membrane candidate for overexpressing SIRPα protein. For convenience, SIRPα-M was used to represent the cell membrane of the SIRPα-RAW@M1 group.



SIRP $\alpha$ -RAW cell membranes were collected after freezing and thawing and were then coated onto nanoparticles by mechanical squeezing through the liposome extruder. To evaluate the vesicle properties following extrusion, empty vesicles and membrane-coated nanoPB were fabricated. First, the empty membrane vesicles were analyzed using a nanoparticle tracking analyzer, and their size was measured using a scanning electron microscope. The size distribution of the membrane vesicles has a main peak at a diameter of 167 nm and a smaller peak at 265 nm (Fig. S3A), suggesting that some fusion of the membrane vesicles may have occurred during the preparation process, producing larger vesicles. The scanning electron microscopy revealed empty membrane vesicle structures having a size of approximately 200 nm (Fig. S3B). The Coomassie brilliant blue staining revealed that in comparison with the protein composition of the whole cell, cytoplasmic, and cell membrane proteins, the vesicles exhibited a protein composition closely resembling that of the cell membrane (Fig. S3C). The presence of SIRP $\alpha$  on the membrane vesicles was also confirmed by Western blotting (Fig. S3D), indicating that the mechanical processing of the liposome extruder during vesicle preparation did not significantly damage the protein content on the membrane, thus preserving the biological function of the vesicles.

The engineered cell membranes were utilised to encapsulate microwave-responsive PB nanoparticles (nanoPB). Nanocubic-like nanoPB were first synthesized according to our previous study [34]. Mechanistically, the microwave excitation of nanoPB induces dielectric loss and spin state alteration of iron ions, generating heat and weakening bond energy, accelerating iron release and promoting ROS generation in cells (Fig. 1A). The successful fabrication of nanoPB was validated by area elemental mapping with a uniform distribution of Fe and Na (Fig. 1B). In comparison with transmission electron microscopy (TEM), it is evident that there is an absence of a membrane-like structure on the surface of nanoPB (Fig. S3E), while a membrane-like structure is present on the surface of SIRP $\alpha$ -M@nanoPB with a thickness of approximately 10 nm (Fig. 1C). The particle size and composition of the coating membrane on nanoPB were also evaluated. The membrane-coating particles had an average size of 200 nm, with peaks at 212 and 306 nm (Fig. 1D). The western blotting also confirmed the presence of membrane proteins and SIRP $\alpha$  on the SIRP $\alpha$ -M@nanoPB (Fig. 1E). The Coomassie brilliant blue staining confirmed that the protein composition of SIRP $\alpha$ -M@nanoPB, obtained through gene engineering, extraction, and coating onto nanoPB, was consistent with that of cell membrane proteins (Fig. 1F).

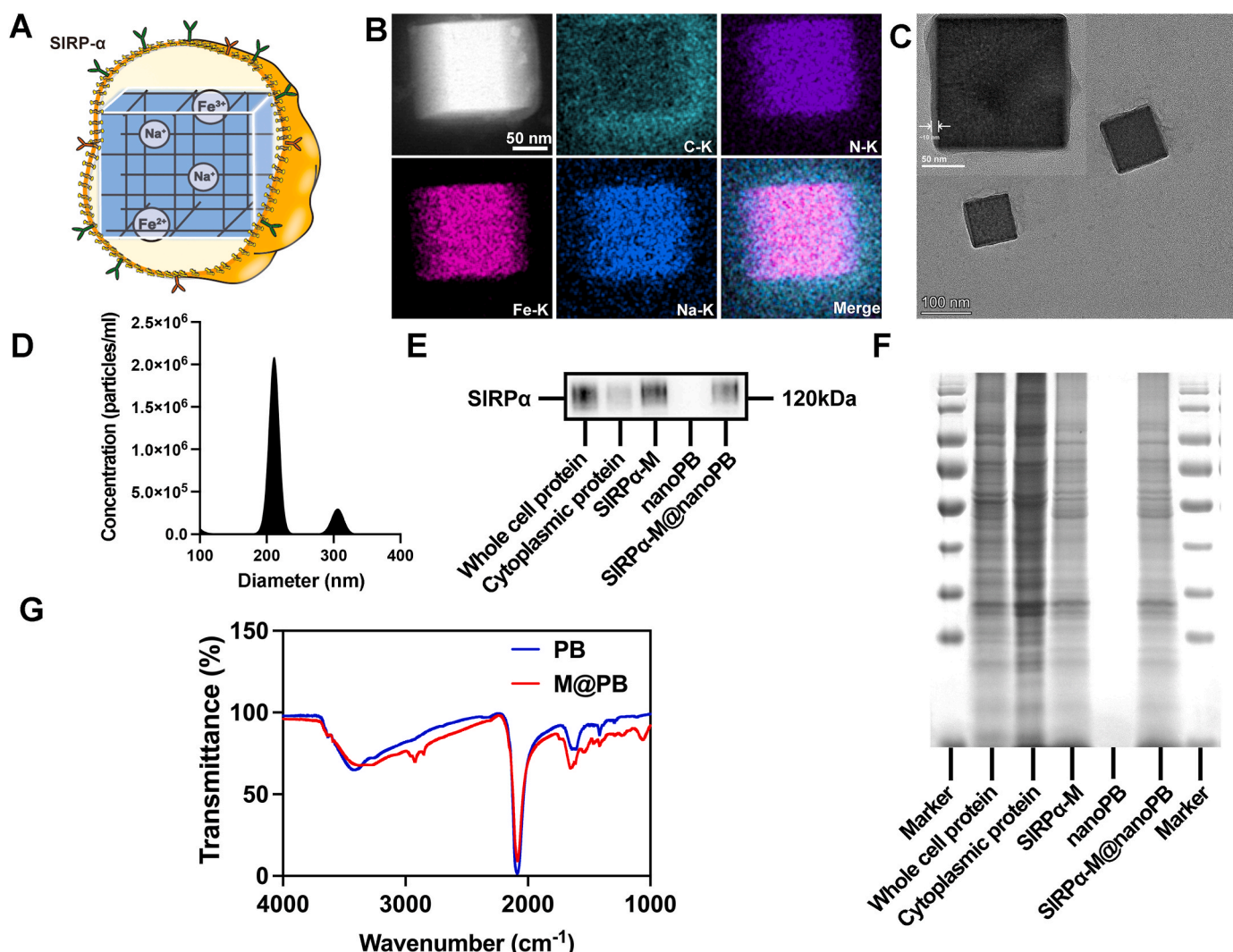


**Fig. 1.** Physical characterization of SIRP $\alpha$ -M@nanoPB. (A) Schema of membrane coating of nanoPB. Cell membranes were isolated from RAW264.7 overexpressed SIRP $\alpha$ . (B) Elemental mapping of SIRP $\alpha$ -M@nanoPB. Scale bar = 50 nm. (C) Transmission electron microscopy (TEM) image of SIRP $\alpha$ -M@nanoPB. Scale bars = 50 nm and 100 nm. (D) Size distribution of NPs before or after membrane coating. (E) Representative proteins of SIRP $\alpha$  protein in engineering macrophage and nanoPB before or after membrane coating using western blotting. (F) Whole protein distribution of engineering cell membrane before and after coating on nanoPB using western blotting. (G) FTIR of nanoPB and SIRP $\alpha$ -M@nanoPB.



FTIR spectroscopy revealed a distinct absorption band at approximately  $2200\text{ cm}^{-1}$ , characteristic for PB, as well as bands indicative of cell membrane components. Thus, it confirmed the presence of engineered cellular membranes on the surface of nanoPB (Fig. 1G).

The resulting membrane-coating nanoPB demonstrated excellent dispersibility in various biological media, including saline, PBS, and DMEM, and they maintained the stability over a period of 1 week (Fig. S4A), which made them suitable for subsequent *in vivo* applications. In addition, TEM images of SIRP $\alpha$ -M@nanoPB stored at  $4^\circ\text{C}$  in PBS and foetal bovine serum (FBS) for a period of seven days were also obtained (Figs. S4B and C). It was ascertained that the cell membrane coating structure of SIRP $\alpha$ -M@nanoPB remained stable.

## 2.2. Microwave responsiveness of SIRP $\alpha$ -M@nanoPB *in vitro* and *in vivo*

As a microwave-responsive material, the structure of nanoPB remains intact even following microwave irradiation (referred to as MW), which allows it to reflect electromagnetic waves and exhibit dielectric loss properties. The MW dissipation determines its ability to absorb microwave radiation and generate heat [34]. To validate the thermal effect after membrane coating, the temperature curves of 0.9 % NaCl, 1 mg/mL nanoPB, and 1 mg/mL SIRP $\alpha$ -M@nanoPB under irradiation microwave at 10 W were obtained using a near-infrared thermal imaging camera (Fig. 2A and B). The nanoPB could significantly increase the temperature compared with that of the saline control group. However, under the same microwave conditions, the heat generation of SIRP $\alpha$ -M@nanoPB is reduced compared with that of nanoPB at an equivalent concentration. This reduction in heat generation is attributable to the weakened absorption of microwave energy by Fe atoms in nanoPB following membrane encapsulation. However, SIRP $\alpha$ -M@nanoPB still exhibits a significant microwave thermal effect compared to the saline control group. Fig. 2C validates the repeated microwave-heating capability of SIRP $\alpha$ -M@nanoPB, indicating there is an excellent reactivity under irradiation as a treatment requirement. To explore the heat generation *in vivo*, an infrared thermal imaging camera was employed to monitor the real-time temperature of tumor-bearing mice during microwave exposure following nanoparticle injection (Fig. 2D and E). The resulting *in vivo* microwave thermal effect was consistent with the results obtained *in vitro*. The microwave thermal effect of SIRP $\alpha$ -M@nanoPB was lower than that of nanoPB but still superior to that of the control group. Importantly, the heated area was constrained in tumor tissue, indicating that this thermal effect of SIRP $\alpha$ -M@nanoPB could effectively eradicate tumor cells through microwave irradiation.

To assess the oxidation capability of SIRP $\alpha$ -M@nanoPB in response to microwave irradiation, degradation experiments were conducted using Rhodamine B (RhB) (Fig. 2F). The absorption of RhB at 553 nm in the control group showed a slight decrease after 10 min of microwave irradiation. Conversely, in both the nanoPB and SIRP $\alpha$ -M@nanoPB groups, the absorption of RhB at 553 nm decreased in a time-dependent manner under microwave irradiation. These results demonstrate the excellent ability of nanoPB to generate ROS when exposed to microwave irradiation, while the presence of the cell membrane coating did not affect the release of ROS into the medium. To quantitatively assess the ROS generation capability of nanoPB and the effect of cell membrane coating, singlet oxygen sensor green was employed as a probe to detect ROS-induced oxidation, producing green fluorescence. The fluorescent signal significantly increased upon microwave irradiation in both nanoPB and SIRP $\alpha$ -M@nanoPB groups, indicating that there was an excellent ability of SIRP $\alpha$ -M@nanoPB to release ROS and the negligible impact of the cell membrane coating on the microwave dynamics process (Fig. 2G).

To investigate the ROS generation capability of SIRP $\alpha$ -M@nanoPB at the cellular level, nonfluorescent 2',7'-dichlorofluorescein diacetate (DCFH-DA) was used as a detection probe as this is oxidized by ROS into green-fluorescent 2',7'-dichlorofluorescein (DCF). Negligible

fluorescence signals were detected in the PBS control, MW-only treated, nanoPB, and SIRP $\alpha$ -M@nanoPB-only groups. However, when PB and SIRP $\alpha$ -M@nanoPB were combined with MW irradiation, a significant increase in green fluorescence was observed, indicating that PB generates a large amount of ROS under MW irradiation. Particularly, treating SIRP $\alpha$ -M@nanoPB with MW produced a stronger green fluorescence than PB with MW. This finding suggests that the presence of SIRP $\alpha$ -M enhances the PB adhesion and targeting of tumor cells (Fig. 2H). It is noteworthy that Fig. 2D demonstrates that nanoPB exhibits a superior microwave thermal effect in comparison to SIRP $\alpha$ -M@nanoPB. However, Fig. 2H demonstrates that the SIRP $\alpha$ -M@nanoPB + MW group produced the most reactive oxygen species in tumour cells. These seemingly contradictory results are not incompatible but rather underscore the distinct therapeutic effects under varying evaluative criteria. While nanoPB demonstrates efficacy in terms of microwave thermal effects, SIRP $\alpha$ -M@nanoPB + MW exhibits superior tumour cell targeting and microwave thermal efficiency. In conclusion, it may be concluded that the anti-tumour ability of SIRP $\alpha$ -M@nanoPB + MW is superior.

## 2.3. SIRP $\alpha$ -M@nanoPB-mediated cytotoxicity profiles and cytocompatibility at the cellular level

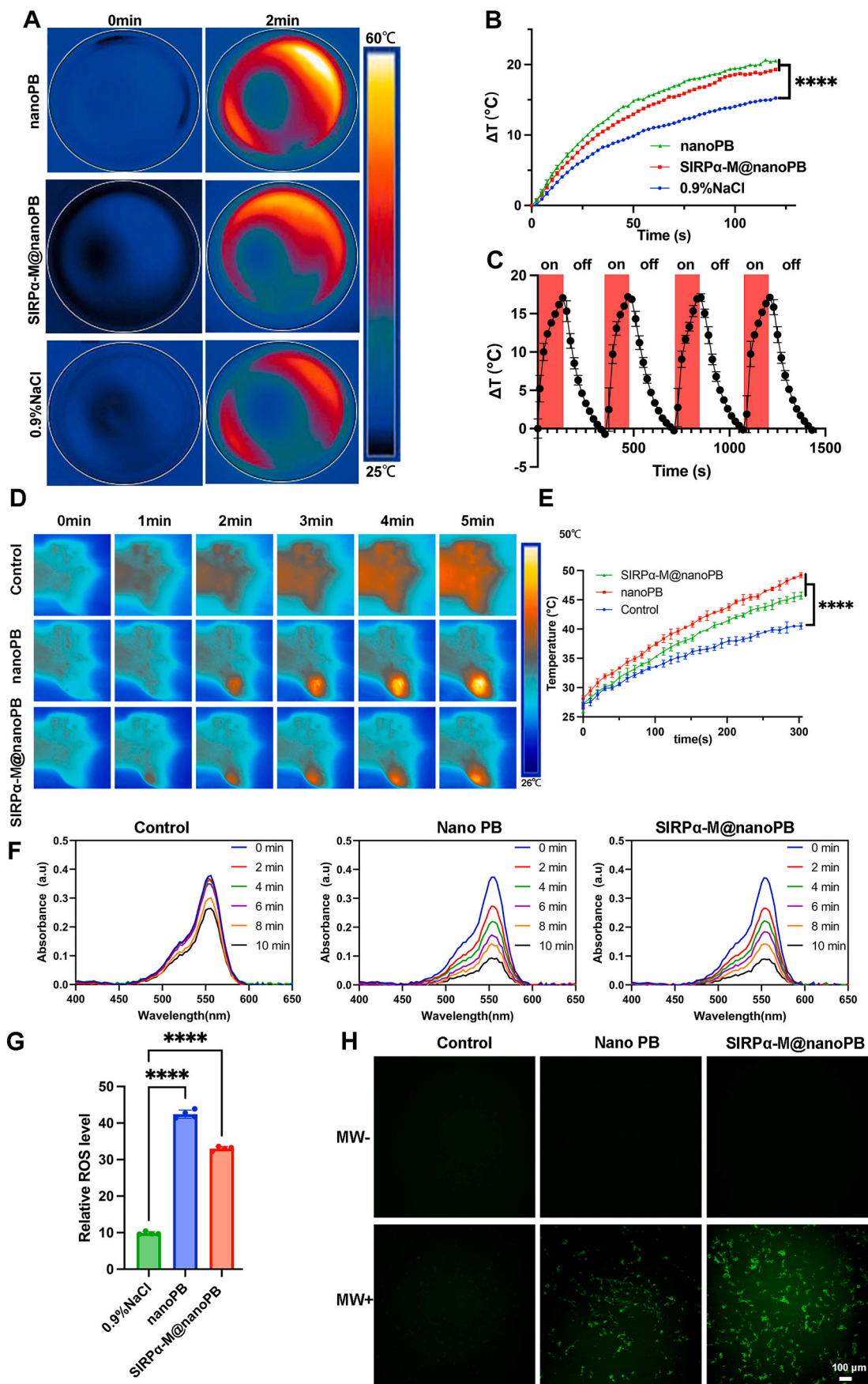
The hemolysis test suggests that PB nanoparticles may cause mild hemolysis, whereas wrapping in macrophage membranes can alleviate this phenomenon, which indicates the favorable biocompatibility of PB nanoparticles and the ability of membrane-wrapped particles to persist in the body steadily (Fig. 3A). Similarly, the CCK-8 assay was employed to examine the cytotoxicity of saline, nanoPB, and SIRP $\alpha$ -M@nanoPB on MSC cells (Fig. 3B). The viability of K7M2 cells decreased with increasing concentration after 24 h of incubation, with an IC<sub>50</sub> of 0.5 mg/mL (Fig. S5A). Microwave irradiation for 5 min further decreased the cell viability in nanoPB-presented groups (nanoPB and SIRP $\alpha$ -M@nanoPB groups). Interestingly, the cell viability of the SIRP $\alpha$ -M@nanoPB group increased with the cell membrane coating, suggesting that the membrane coating protected the cells from the toxicity of NPs. However, the SIRP $\alpha$ -M@nanoPB group still exhibited a strong cytotoxic effect with microwave irradiation, indicating that the cell membrane coating had minimal influence on the microwave dynamics and thermal effect of nanoPB (Fig. 3C).

To assess the efficacy of killing tumor cells directly, a Live/Dead assay was performed. Calcein-AM was used to label live cells green, while PI was used to stain dead cells red. The SIRP $\alpha$ -M@nanoPB group consistently showed more green fluorescence than the PB group. However, microwave irradiation increased the red fluorescence in both groups. The results confirm the strong tumor-killing effect of SIRP $\alpha$ -M@nanoPB and its excellent compatibility with cells when exposed to microwave irradiation (Fig. 3D).

Conversely, minimal cytotoxicity was found in the proliferation of C3H10 cells following incubation for 24 h with a high concentration of 1 mg/mL. The Live/Dead assay confirmed the high cell compatibility for normal cells (Fig. S5B).

## 2.4. Tumor-targeted and immune activation of SIRP $\alpha$ -M@nanoPB

The SIRP $\alpha$ -M@nanoPB was designed to selectively bind to CD47 expressed on OS tumor cells and be internalized by TAMs, inducing M1 polarization in the TME [35,36]. We conducted immunofluorescence colocalization analysis to investigate the binding of membrane vesicles to K7M2 cells (Fig. 4A, S6A). The SIRP $\alpha$  on the membrane surface was labeled with red fluorescence, while the CD47 on the surface of K7M2 cells was labeled with green fluorescence. The merged image illustrates the presence of yellow-overlapping regions, which indicate spatial colocalization between the two proteins. A coimmunoprecipitation (CO-IP) assay was conducted to investigate the interaction between SIRP $\alpha$  on the macrophage membrane and CD47 on OS tumor cells. Following overnight incubation, the SIRP $\alpha$  was pulled down using a GFP



(caption on next page)

**Fig. 2. Microwave-responsive thermal and dynamics of SIRP $\alpha$ -M@nanoPB.** (A) Representative real-time infrared thermal imaging of saline, nanoPB, and SIRP $\alpha$ -M@nanoPB under MW irradiation (1 mg/mL, 0.28 Wcm<sup>-2</sup> for 5 min). (B) Temperature rise curve of different samples with MW irradiation. (C) Temperature rise cycle of SIRP $\alpha$ -M@nanoPB under MW irradiation (0.28 Wcm<sup>-2</sup>) for 2 min followed by natural cooling. (D) Representative *in vivo* real-time infrared thermal imaging of saline, nanoPB, and SIRP $\alpha$ -M@nanoPB injected into knee cavity under MW irradiation (1 mg/mL, 0.28 Wcm<sup>-2</sup> for 5 min). (E) Temperature rise curve of different samples with MW irradiation *in vivo*. (F) UV-vis spectra of saline, nanoPB, and SIRP $\alpha$ -M@nanoPB irradiated by MW (0.28 Wcm<sup>-2</sup>) with varied concentrations for 10 min. (G) Quantitative analysis of ROS production of saline, nanoPB, and SIRP $\alpha$ -M@nanoPB using singlet oxygen sensor. (H) Representative fluorescence images of intracellular ROS generation in tumor cells treated with saline, nanoPB, and SIRP $\alpha$ -M@nanoPB under MW irradiation (1 mg/mL, 0.28 Wcm<sup>-2</sup> for 5 min). Scale bar = 100  $\mu$ m \**p* < 0.05, \*\**p* < 0.01, \*\*\**p* < 0.001, \*\*\*\**p* < 0.0001.

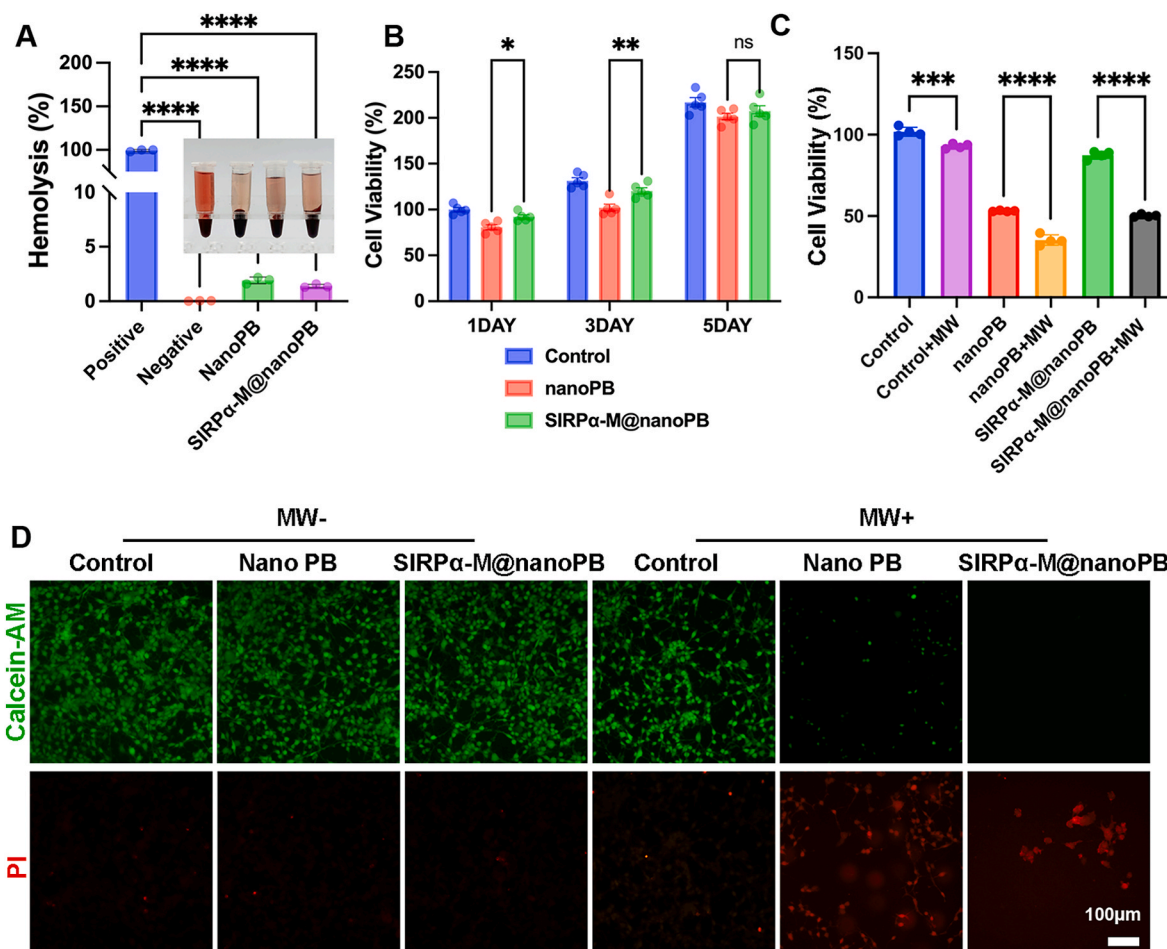


**Fig. 3. Cytocompatibility of SIRP $\alpha$ -M@nanoPB.** (A) Hemolysis ratio of fresh human blood incubated with saline, nanoPB, and SIRP $\alpha$ -M@nanoPB (1 mg/mL). And the nested picture was corresponding photographs. (B) Cell proliferation of MSCs treated with saline, nanoPB, and SIRP $\alpha$ -M@nanoPB (1 mg/mL) for 1d, 3d and 5d using CCK8 assay. (C) Cell viability of K7M2 cells treated with saline, nanoPB, and SIRP $\alpha$ -M@nanoPB (1 mg/mL) under MW irradiation. (D) Live-dead assay of K7M2 cells treated with saline, nanoPB, and SIRP $\alpha$ -M@nanoPB (1 mg/mL) under MW irradiation. Scale bar = 100  $\mu$ m \**p* < 0.05, \*\**p* < 0.01, \*\*\**p* < 0.001, \*\*\*\**p* < 0.0001.

antibody, and the supernatants were subjected to immunoprecipitation for western blotting. The results clearly indicate that CD47 was successfully pulled down by SIRP $\alpha$  compared to the control results (Fig. 4B). This finding supports the notion that SIRP $\alpha$  can effectively bind to CD47 on tumor cells. In addition, the expression of CD47 in K7M2 tumour cells was reduced using RNA interference (RNAi) technology, and the knockdown efficiency of CD47 has been confirmed by RT-PCR and WB. (Figs. S6B–D). The function of siCD47 is to block the CD47-SIRP $\alpha$  signalling pathway, thereby activating macrophages to engulf tumour cells. In a subsequent experiment, siCD47 was utilised as a group to ascertain whether the reduction of CD47 protein in K7M2 can effectively disrupt receptor-ligand interactions between macrophages and tumor cells.

The phagocytic effects of BMDMs and RAW264.7 on K7M2 tumour cells following different treatments were evaluated by live-cell fluorescence imaging and flow cytometry (Fig. 4C–D, S7). In the BMDMs and

K7M2 cell fluorescence experiments, K7M2 cells were labeled with DiO green fluorescent probes, while BMDMs cells were labeled with Dil red fluorescent probes. The simultaneous green and red fluorescence emitted by cells is an indicator of phagocytosis activity of macrophages. The SIRP $\alpha$ -M coating effectively alleviated phagocytic inhibition, and real-time surveillance video and flow cytometry confirmed that BMDMs macrophages regained the ability to kill tumour cells after adding the modified cell membrane. A similar experimental outcome is demonstrated in Fig. 4C following repeated flow cytometry tests utilizing RAW264.7 macrophages. The results demonstrated that SIRP $\alpha$  on the coating cell membrane could effectively restore the phagocytosis of macrophages on tumor cells.

Furthermore, live-cell imaging was utilised to capture time-lapse images of K7M2 tumour cells (labeled in green) and BMDMs (labeled in red) over a period of 4 h (Fig. 4E and S8). This facilitated the observation of the dynamic changes in the behaviour of the macrophages. To



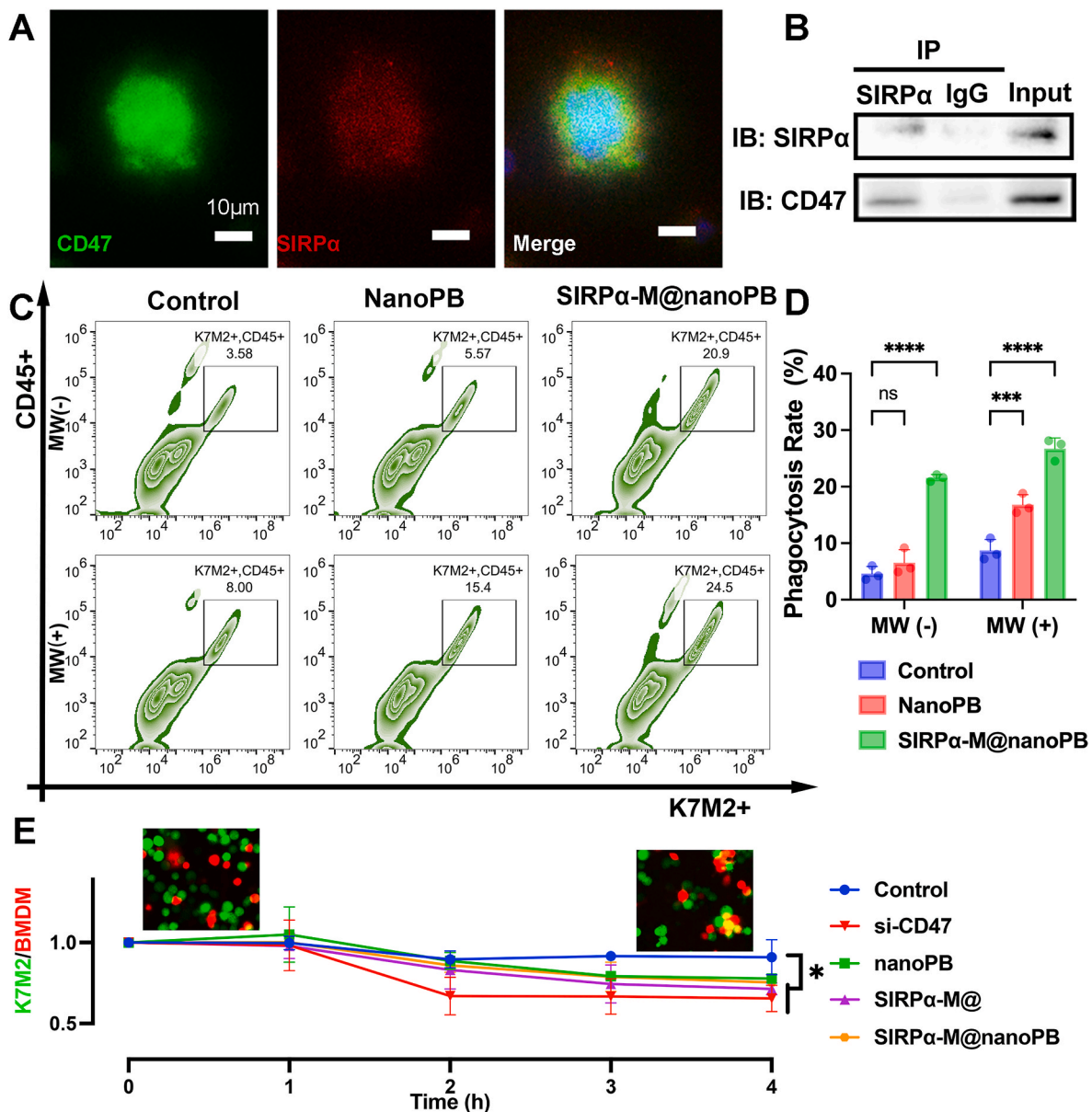
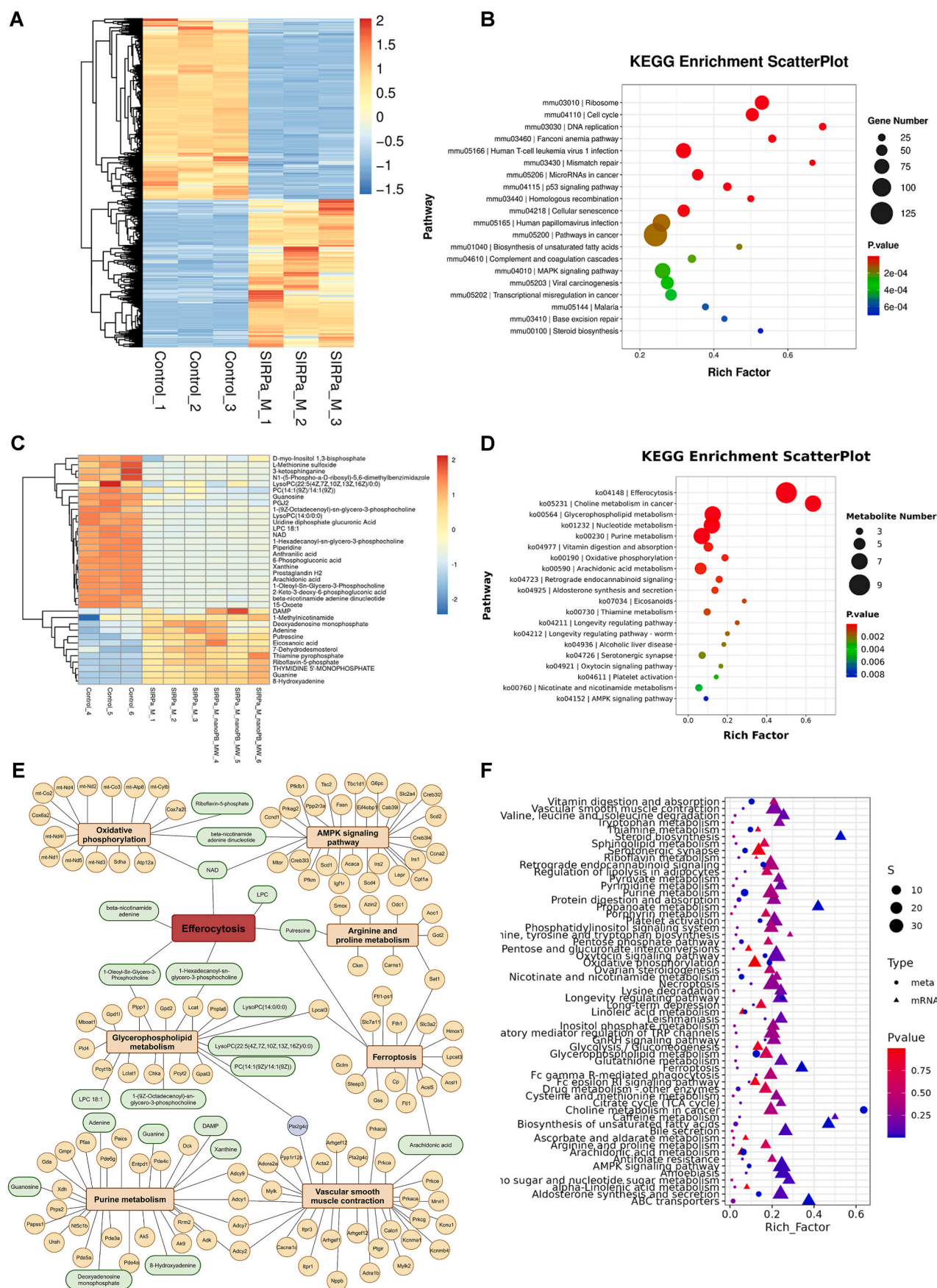


**Fig. 4.** Tumor targeting and macrophage phagocytic activity restoration by SIRPα-M@nanoPB. (A) Representative fluorescent images depicting the binding of SIRPα labeled macrophage membrane vesicles (Red) and CD47 labeled K7M2 cells (Green). Scale bar = 10 μm. (B) Co-immunoprecipitation (Co-IP) assays demonstrating interactions of CD47 and SIRPα in K7M2 cells treated with SIRPα-M@nanoPB. (C–D) Flow cytometry analysis and quantification of macrophage phagocytosis when treated with saline, nanoPB, and SIRPα-M@nanoPB (1 mg/mL) under MW irradiation. CD45 was used to label macrophages with red fluorescence, while K7M2 expressed FITC protein exhibited green fluorescence. K7M2<sup>+</sup>CD45<sup>+</sup> indicated macrophages phagocytizing tumor cells. (E) Real-time monitoring of macrophage (red) phagocytosis for tumor cells (green) treated with saline, nanoPB, SIRPα-M vesicles (SIRPα-M@), and SIRPα-M@nanoPB (1 mg/mL). Tumor cells knocked down with CD47 (si-CD47) were used as a negative control. And the nested picture was representative confocal microscopic images. \**p* < 0.05, \*\**p* < 0.01, \*\*\**p* < 0.001, \*\*\*\**p* < 0.0001.

quantitatively assess the phagocytic activity, the ratio of green-fluorescent to red-fluorescent cells was calculated at each time point, with the ratio at 0 h serving as calibration data. The results illustrate that the si-CD47 group had the lowest phagocytic ratio, followed by that of the SIRPα-M@ group. The intervention with siCD47 and SIRPα-M@ nanoparticles has effectively diminished CD47 expression, thereby reducing the immune evasion capability of K7M2 cells, which facilitates the recognition and phagocytosis of K7M2 cells by BMDM. This finding indicates that reducing or competing with CD47 binding can effectively enhance macrophage phagocytic ability.

## 2.5. Investigation of the underlying antitumor mechanism

To elucidate the potential genetic mechanisms by which SIRPα-M@nanoPB inhibits the survival of OS cells, we performed a transcriptomic analysis comparing the SIRPα-M@nanoPB-treated group with the control group. Hierarchical clustering of the heat map revealed 2288 upregulated genes ( $\log_2\text{FC} \geq 1$ ,  $q < 0.05$ ) and 2794 downregulated genes ( $\log_2\text{FC} \geq 1$ ,  $q < 0.05$ ) between the two groups (Figure S9A, Fig. 5A). KEGG enrichment bubble plot analysis (Fig. 5B) showed that the differentially expressed genes (DEGs) were primarily enriched in pathways related to cell necrosis, such as the Cell cycle, p53 signaling pathway, and Cellular senescence. Additionally, inflammation-related pathways, including the TNF signaling pathway, Th1 and Th2 cell



(caption on next page)

**Fig. 5. Transcriptomics and non-targeted metabolomics analysis.** (A) Heatmap of differentially expressed genes in the SIRPa-M@nanoPB group compared to the Control group. Different colors represent different levels of gene expression, with colors ranging from blue (low expression) to red (high expression); red indicates highly expressed genes, and blue indicates lowly expressed genes. (B) KEGG enrichment analysis of differentially expressed genes, ranked by p-value in ascending order ( $p < 0.05$ ). (C) Heatmap of differentially expressed metabolites in the non-targeted metabolomics analysis (VIP > 1,  $p < 0.05$ ). The color intensity is proportional to the significance of the change (red for up-regulated and blue for down-regulated). Rows and columns correspond to metabolites and samples, respectively. (D) KEGG enrichment analysis of differentially expressed metabolites, ranked by p-value in ascending order ( $p < 0.05$ ). (E) Relationship network diagram of KEGG enrichment for both transcriptomics and metabolomics. Circles represent differentially expressed genes, triangles represent differentially expressed metabolites, and squares show pathways commonly enriched in both omics. (F) KEGG enrichment common pathways of transcriptomics and metabolomics are displayed, where dots represent transcriptomics, triangles represent metabolites, and the size of the shapes reflects the number of differentially expressed genes and metabolites. The color represents the enrichment p-value.

differentiation, and IL-17 signaling pathway, were significantly up-regulated. Pathways related to classical tumor-associated pathways, such as the MAPK signaling pathway, PI3K-Akt signaling pathway, ECM-receptor interaction, Cell adhesion molecules, and AMPK signaling pathway, were inhibited. Moreover, significant enrichment was found in metabolic pathways related to tumor survival, metastasis, and cell necrosis, such as Fatty acid metabolism, Lysine degradation, Glycosaminoglycan degradation, Glyoxylate and dicarboxylate metabolism, and Glutathione metabolism. These findings suggest that SIRPa-M@nanoPB may exert its anti-tumor effects by modulating the metabolic characteristics of tumor cells.

To further validate the regulatory effects of SIRPa-M@nanoPB on OS cell metabolism, we conducted an untargeted metabolomic analysis using LC-MS, identifying a total of 408 metabolites, with 72 upregulated and 336 downregulated (Fig. S9B). The differentially expressed metabolites were primarily enriched in pathways (Fig. 5C and D) such as Efferocytosis, Choline metabolism in cancer, Glycerophospholipid metabolism, Nucleotide metabolism, and Purine metabolism. Notably, significant enrichment in Efferocytosis suggests a potential mechanism by which SIRPa-M@nanoPB combats OS. Efferocytosis is the physiological process of phagocytosing and clearing apoptotic cells, regulating inflammatory responses, and the immune environment to promote cancer cell immune evasion, thereby controlling tumor development and progression. This process strikes a delicate balance through the coordination of "find-me," "eat-me," and "don't-eat-me" signals, influencing tumor cell proliferation, invasion, metastasis, and angiogenesis while modulating adaptive responses and resistance to anti-tumor therapies. Therefore, molecules and pathways related to Efferocytosis could be potential targets for anti-tumor treatments [37]. SIRPa-M@nanoPB activates Efferocytosis in tumor cells and, when combined with CD47-SIRPα blockade immunotherapy and microwave hyperthermia, can enhance therapeutic efficacy. The combination allows for easier recognition and phagocytosis of tumor cells by the immune system by blocking the "don't-eat-me" signal on cancer cells. Through promoting tumor cell clearance and adjusting the local immune environment, the integrated approach offers a promising and effective strategy for the treatment of OS, providing valuable insights for developing more precise anti-tumor therapies.

Furthermore, through integrated analysis of the transcriptomic and metabolomic data, as shown in the Venn diagram in Fig. S9C, we found common enrichment in pathways such as Biosynthesis of unsaturated fatty acids, Ferroptosis, and the AMPK signaling pathway (Fig. 5E). The node network analysis indicates that efferocytosis is closely connected to the significantly regulated pathways (Fig. 5F). Drawing upon the findings of the aforementioned analysis, we employed real-time quantitative fluorescent PCR (qRT-PCR) to ascertain the mRNA expression levels of AMPK, FASN, ACACA, SCD, JNK and P53 in K7M2 cells subjected to treatment with SIRPα-M@nanoPB + MW (Fig. S9D). The results obtained demonstrated significant alterations in the expression levels of these genes. These results elucidate that these pathways may constitute the intrinsic mechanisms by which SIRPa-M@nanoPB regulates OS cell metabolism and exerts its anti-tumor effects.

## 2.6. *In vivo* antitumor effect of SIRPα-M@nanoPB

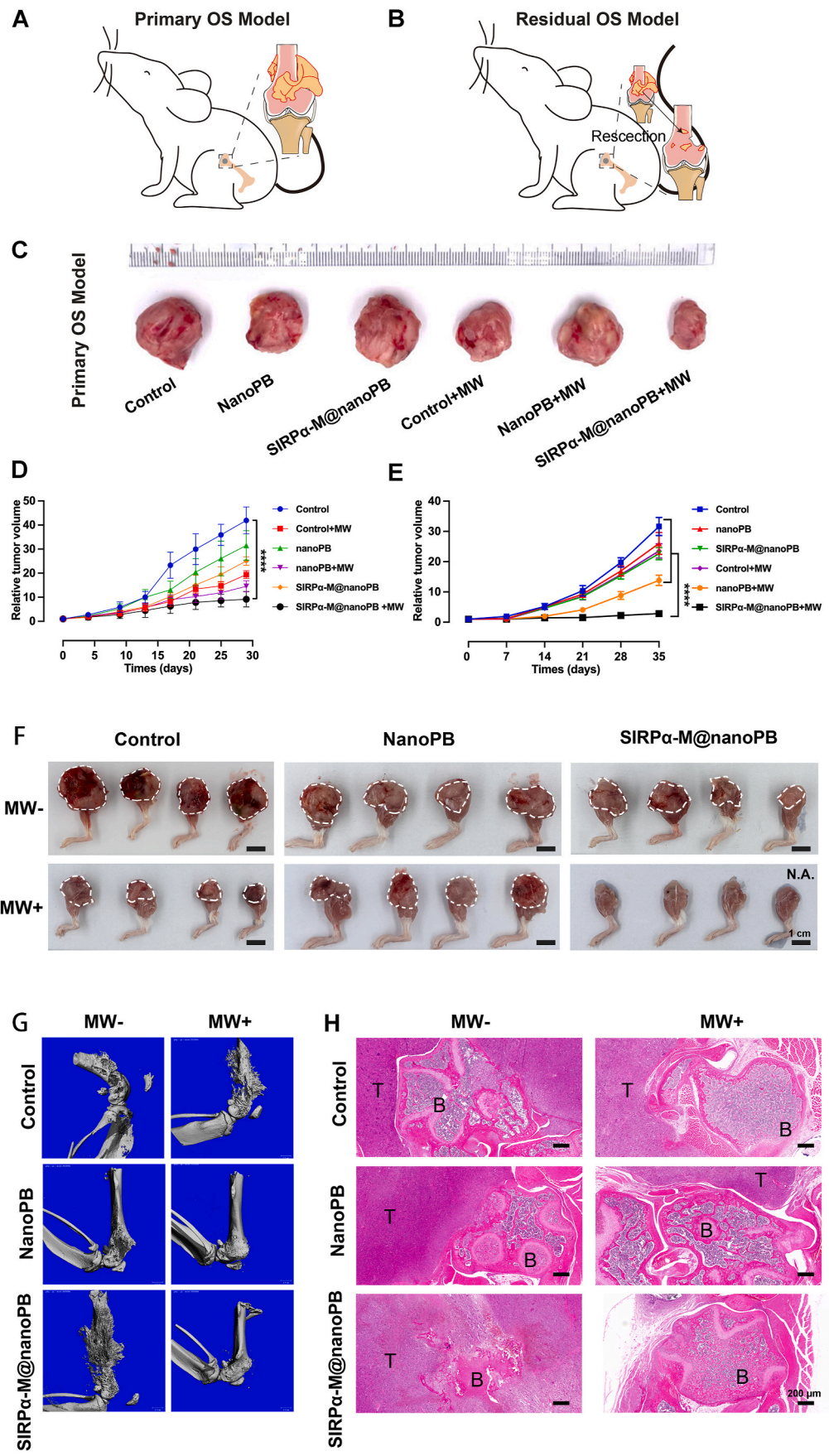
The microwave ablation-immunotherapeutic effect of SIRPα-M@nanoPB was evaluated using a femoral orthotopic osteosarcoma mouse model. We used two types of models to simulate diverse clinical cases of primary and residual tumor groups (Fig. 6A and B).

For the original tumor model, the treatment was performed when the tumor volume was approximately 100 mm<sup>3</sup>. The mice were divided into six groups (PBS control, NanoPB, SIRPα-M@nanoPB, PBS + MW, NanoPB + MW, and SIRPα-M@nanoPB + MW). The MW irradiation was conducted on the first 3 days at the beginning of treatment, and a thermal camera was used to investigate the thermal effect of local tissue to avoid overheating. As shown in Fig. 6C and D, in the PBS control group, the tumor volume exhibited rapid growth throughout all observed time points. Conversely, the MW and PB groups demonstrated a noticeable inhibitory effect, likely attributable to the thermal killing and cytotoxic impact of NPs on tumor cells. Among the different groups, the SIRPα-M@nanoPB + MW group exhibited the slowest tumor growth, indicating superior tumor-inhibitory effects. This improved therapeutic outcome is attributable to the synergistic effect of the thermal killing ability of nanoPB and immune suppression relief provided by the SIRPα-M coating membrane. The SIRPα overexpression on the coating membrane competitively binds to CD47 on tumor cells, effectively blocking the don't-eat-me signal pathway and restoring the macrophage function. Furthermore, all groups exhibited comparable weight loss without any significant difference, indicating minimal side effects and excellent SIRPα-M@nanoPB biocompatibility (Fig. S10). These findings are consistent with the *in vitro* cytocompatibility results (Fig. 3B). Apart from the Control group, the other groups demonstrated varying levels of tumor growth inhibition. However, none of these groups exhibited a complete cessation of tumor growth.

In the residual tumor model (Fig. 6B and S11), the NP treatment was administered concurrently with the implantation of tumor tissue. Mice were then divided into six groups (PBS control and nanoPB and SIRPα-M@nanoPB with or without MW treatment). The MW irradiation was administered during the initial 3 days of the treatment regimen. To ensure the safety of mice and assess the thermal effects, a thermal camera was employed to monitor the local knee area and prevent any potential overheating issues. Consistent with the primary tumor model, the PBS control group exhibited rapid tumor growth throughout the entire observation period. However, the groups treated with NP and MW showed a notably stronger inhibitory effect. The most marked outcome was the complete eradication of tumors observed in the SIRPα-M@nanoPB group when MW stimulation was applied (Fig. 6E and F).

Bone resorption is a crucial factor in tumor progression, and evaluating bone destruction at the defect site can reflect the clearance of tumor cells. Representative micro-CT reconstruction images (Fig. 6G) demonstrated that in the absence of MW, the femur in the control group had significant bone destruction not limited to the initial modeling defect site. The bone destruction in the PB group was limited to the modeling defect site and its surroundings, suggesting the inhibitory effect of nanoPB on tumor growth. Surprisingly, significant bone destruction reappeared in the SIRPα-M@nanoPB group, which may be due to the membrane wrapping reducing the effect of PB on tumors, and the relief of immunosuppression on macrophages by the cell membrane





(caption on next page)

**Fig. 6.** *In vivo* anti-tumor effect of SIRP $\alpha$ -M@nanoPB in primary and residual models. (A) Schematic illustration of animal surgery procedure for establishing primary tumor modeling. (B) Schematic illustration of animal surgery procedure for establishing residual tumor modeling. (C) Macroscopic view of harvest tumor samples in different groups. (D) Relative tumor growth curve of primary model treated with saline, nanoPB, and SIRP $\alpha$ -M@nanoPB (1 mg/mL) under MW irradiation for 30 days. Normalized tumor volume indicates the relative volume when the tumor volume at day 0 (at the start of tumor implantation) is set to 0. (E) Relative tumor growth curve of residual model treated with saline, nanoPB, and SIRP $\alpha$ -M@nanoPB (1 mg/mL) under MW irradiation for 35 days. (F) Macroscopic view of harvest tumor samples with bone tissue in different groups. White dots indicate the region of tumor in mice femur. Scale bar = 1 cm (G–H) Micro-CT and H&E staining reconstruction of harvest tumor samples with bone tissue in different groups. Scale bar = 200  $\mu$ m \* $p$  < 0.05, \*\* $p$  < 0.01, \*\*\* $p$  < 0.001, \*\*\*\* $p$  < 0.0001.

alone cannot inhibit tumor growth. Conversely, under MW treatment, bone destruction was still present in the control group, but both nanoPB and SIRP $\alpha$ -M@nanoPB groups showed regeneration and repair at the modeling bone defect site. The HE staining showed similar results (Fig. 6H). Furthermore, in order to estimate the *in vivo* biocompatibility of each group, major organs (heart, liver, spleen, lung, and kidney) were obtained from mice and sectioned for H&E staining (Fig. S12). The results of this staining demonstrated that SIRP $\alpha$ -M@nanoPB + MW did not result in any discernible damage to the major organs.

## 2.7. SIRP $\alpha$ -M@nanoPB mediated antitumor immune response

Flow cytometry and immunofluorescence staining were employed to investigate macrophage polarization and T-cell activation. This helped to explain the mechanisms behind the antitumor immune response facilitated by SIRP $\alpha$ -M@nanoPB in conjunction with microwave irradiation.

The M1 and M2 macrophage infiltration in the treated tumor was collected and analyzed via flow cytometry. The results demonstrated a polarization shift toward M1 in both the nanoPB + MW and SIRP $\alpha$ -M@nanoPB + MW treated groups (Fig. 7A–C). Notably, the most significant effect was observed in the SIRP $\alpha$ -M@nanoPB + MW group, and this was attributable to synergistic mechanisms that stimulate an antitumor immune response. Additionally, harvested samples were used for T-cell activation analysis, revealing a predominant accumulation of CD8<sup>+</sup> T cells in the tumor tissue as opposed to that of CD4<sup>+</sup> T cells (Fig. 7D–F). CD4 and CD8 are two subgroups of T lymphocytes that play different roles in the immune system. CD4 cells are responsible for helping to activate other immune cells in order to combat pathogens. In contrast, CD8 cells are responsible for the direct destruction of infected cells. An increase in CD8<sup>+</sup> T cells is often associated with a state of immune activation in the body. The present experiment demonstrated that the proliferation of CD8<sup>+</sup> T cells may be due to the regulation of immune status by SIRP $\alpha$ -M@nanoPB + MW, which enhances the ability to fight against tumors.

Immunofluorescence (IF) analysis of CD11b revealed that the mean fluorescence intensity increased upon treatment with nanoPB and microwave irradiation, with the highest activation observed in the SIRP $\alpha$ -M@nanoPB + MW group, suggesting synergistic effects in promoting macrophage accumulation (Fig. 8A). Furthermore, representative IF images of iNOS and CD206 demonstrated a significantly higher iNOS/CD206 ratio in the nanoPB + MW and SIRP $\alpha$ -M@nanoPB + MW groups than in others, which is indicative of M1 polarization and relief of macrophage suppression (Fig. 8B). Interestingly, the accumulation of CD8<sup>+</sup> T cells was observed in the SIRP $\alpha$ -M@nanoPB + MW group (Fig. 8C).

Our findings illustrate that SIRP $\alpha$ -M@nanoPB can induce thermal and immunogenic cell death to modulate macrophage polarization with subsequent enhancement of T-cell activation. This process mitigates immune suppression and promotes the conversion of "cold" into "hot" tumors."

## 3. Discussion

Numerous studies have confirmed that the TME exhibits immune-suppressive characteristics [38]. TAMs play a crucial role in tumor initiation and the formation of an immune-suppressive microenvironment, and tumor metastasis in patients with OS [39]. Osteosarcoma cells

have been shown to release interleukin-34 (IL-34) and colony-stimulating factor 1 (CSF-1) [40], which promote angiogenesis and recruit M2-type TAMs to the tumor tissue. Notably, these M2-type macrophages are correlated positively with immune-suppressed T-cell subsets, ultimately exacerbating immune suppression by disrupting T-cell proliferation and thereby creating a favorable environment for tumor progression [41]. The objective of bone tumor research is to break the immune-suppressive cycle in OS tumors. CD47, a transmembrane glycoprotein abundant in OS cells, interacts with SIRP $\alpha$  on macrophages, thus suppressing phagocytic function and enabling immune escape. The binding of CD47 to SIRP $\alpha$  sends a don't-eat-me signal to macrophages. However, CD47 blockers can enhance macrophage phagocytosis of OS cells and inhibit OS cell invasiveness and lung metastasis [42,43]. Several studies have employed nanoparticles or exosomes to deliver CD47 antibodies that can block the CD47-SIRP $\alpha$  checkpoint and potentially treat solid tumors [44]. Considering the high cost of antibodies, genetic engineering for the overexpression of target proteins in live cells is a more cost-effective approach. An SIRP $\alpha$ -overexpressing macrophage cell line could be constructed through lentiviral transfection, and the M1 polarization was maintained upon LPS stimulation. The marked role of tumor-intrinsic SIRP $\alpha$  has been revealed in enhancing antitumor immunity in contrast to its well-established function as a major inhibitory immune regulator in macrophages. Depleting SIRP $\alpha$  on intra-tumoral macrophages facilitates the infiltration of tumor-specific cytotoxic T cells, NK cells, and inflammatory neutrophils [45]. Therefore, regulating SIRP $\alpha$  and blocking the CD47-SIRP $\alpha$  checkpoint could be a potential focus of future cancer therapy research.

Despite the effectiveness of immune checkpoint inhibitors in other malignancies, their application in OS often leads to a high rate of failures or severe side effects, which leads to poorer outcomes [46]. Thus, synergistic therapy is preferred in the treatment of OS. Thermal therapy is a promising field when it comes to treating various tumors, particularly in achieving low-temperature and targeted tumor ablation. Light-responsive thermal therapy has been extensively studied and numerous designs were examined, but the limited penetration distance cannot reach deep lesions in bone tissue [47]. Alternatively, microwave-responsive particles are more suitable in these clinical cases because of the greater tissue penetration. Our team has worked in this field for a long time and designed microwave-responsive materials autonomously. PB and its analogs exhibit stable structures, adjustable sizes, controllable morphologies, rich modification methods, and excellent physicochemical properties with excellent biocompatibility [48]. Our previously published work demonstrated that the incorporation of Na<sup>+</sup> ions can enhance microwave responsibility [49]. However, the cytotoxicity of nanoparticles and their lack of tumor-targeting capabilities limit their potential for effective tumor therapy *in vivo*. Cell membrane-coated nanoparticles enhance the circulatory stability of nanoparticles and provide them with additional biological functionalities [50]. In addition to cell membranes derived from tumor cells, NK cells, and endothelial cells, macrophages are ideal candidates for membrane coating of nanoparticles [51–53]. Macrophage membranes protect nanoparticles from being engulfed by immune cells and accurately recognize antigens. This characteristic enables them to specifically target inflamed tissue or tumor sites [54]. This study utilized macrophage membranes overexpressing SIRP $\alpha$  following M1 polarization to coat nano PB, thus producing the innovative microwave-responsive SIRP $\alpha$ -M@nanoPB. This not only reduced the

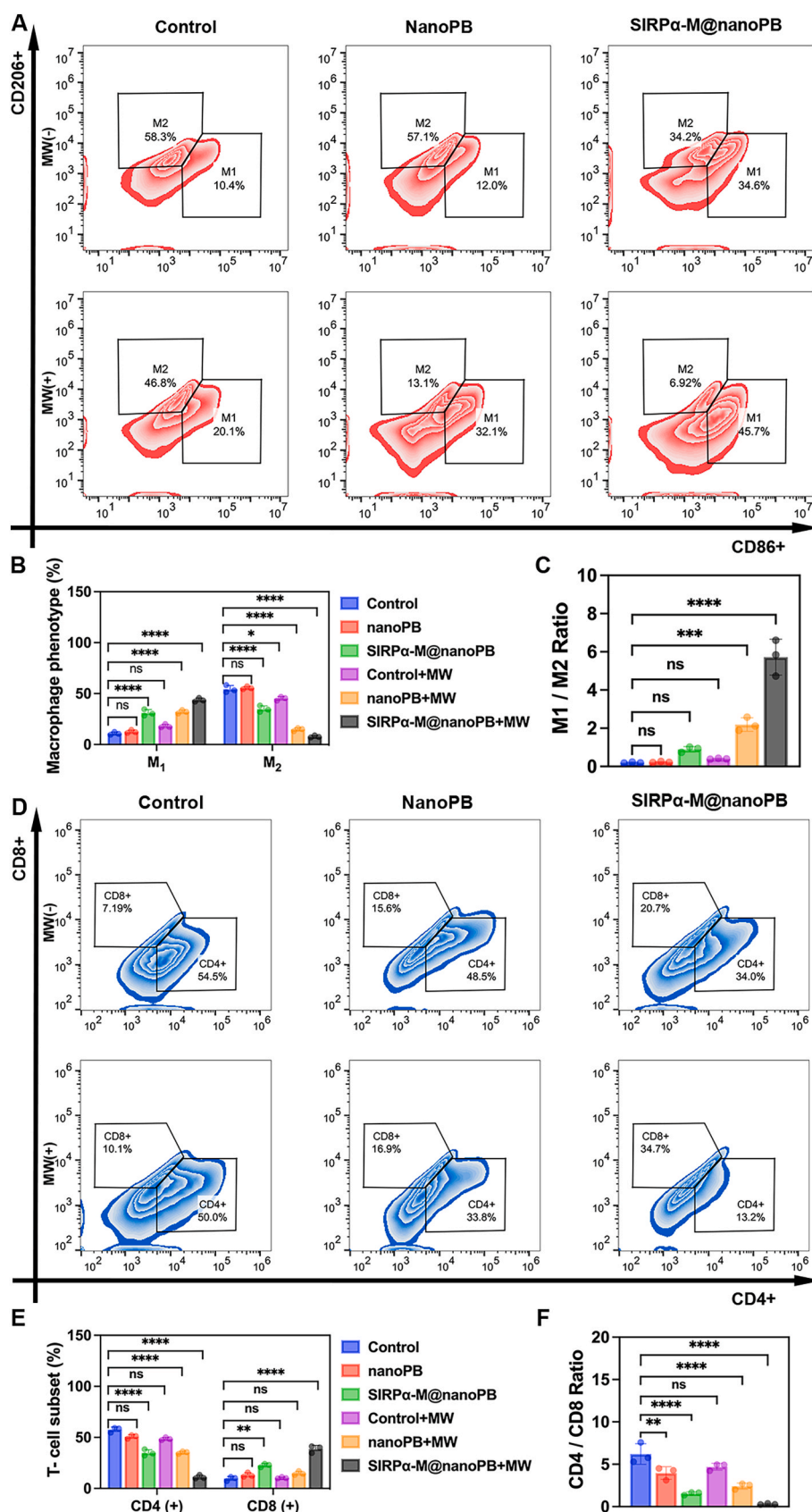


**Fig. 7.** In vivo assessment of immune activation of SIRPα-M@nanoPB using flow cytometry. (A–C) Analysis and quantification of macrophage polarization in tumors treated with saline, nanoPB, and SIRPα-M@nanoPB (1 mg/mL) under MW irradiation. M1 macrophages are indicated by CD86<sup>+</sup>CD206<sup>+</sup>, while M2 macrophages are indicated by CD86<sup>−</sup>CD206<sup>+</sup>. (D–F) Analysis and quantification of CD4<sup>+</sup> and CD8<sup>+</sup> T cells in tumors treated with saline, nanoPB, and SIRPα-M@nanoPB (1 mg/mL) under MW irradiation. CD4 T cells are indicated by CD4<sup>+</sup>CD8<sup>−</sup>, while CD8 T cells are indicated by CD4<sup>−</sup>CD8<sup>+</sup>. \**p* < 0.05, \*\**p* < 0.01, \*\*\**p* < 0.001, \*\*\*\**p* < 0.0001.



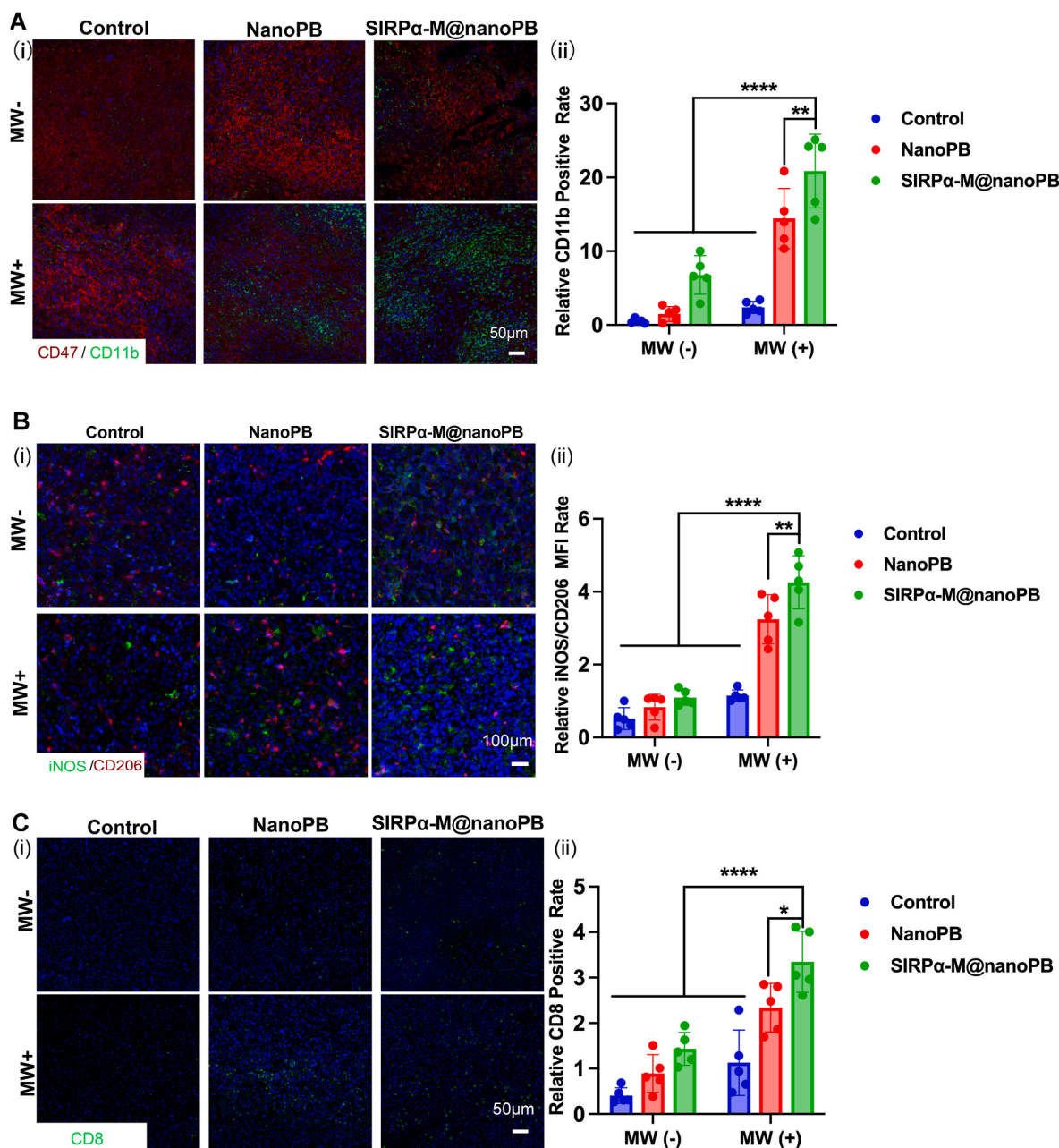


**Fig. 8.** Immunofluorescent (IF) staining of *in vivo* histological sections to assess immune activation by SIRPα-M@nanoPB. (A) Macrophage infiltration and activation in tumor tissue treated with saline, nanoPB, and SIRPα-M@nanoPB (1 mg/mL) under MW irradiation. (i) Representative IF images depicting CD11b positivity to evaluate macrophage activation and CD47 positivity to label OS cells. Scale bar = 50 μm. (ii) Quantitative analysis of CD11b expression. (B) Macrophage polarization in tumor tissue treated with saline, nanoPB, and SIRPα-M@nanoPB under MW irradiation. (i) Representative IF images illustrating iNOS for M1 macrophages and CD206 for M2 macrophages. Scale bar = 100 μm. (ii) Quantitative analysis of iNOS/CD206 expression to evaluate M1 polarization in different groups. (C) T cell activation in tumor tissue treated with saline, nanoPB, and SIRPα-M@nanoPB under MW irradiation. (i) Representative IF images showing CD4 positive cells for CD4 T cells and CD8 positive cells for CD8 T cells. Scale bar = 50 μm. (ii) Quantitative analysis of CD8/CD4 expression to evaluate T cell activation in different groups. \* $p < 0.05$ , \*\* $p < 0.01$ , \*\*\* $p < 0.001$ , \*\*\*\* $p < 0.0001$ .

immunogenicity of the material and improved its biocompatibility, but also increased its targeting toward tumor cells.

Residual tumor models offer a more accurate representation of clinical scenarios than primary tumor models, given that surgical intervention remains the gold standard for treating OS [55,56]. Undetected small metastatic foci play a significant role in tumor recurrence [57]. Following surgery, the application of innovative membrane-encapsulated nanoparticles as a preventive measure shows promise in precisely targeting and eliminating potential tumor cells through immunosuppression relief and microwave thermal effects. For

clinical translation, during the preoperative chemotherapy phase for patients with OS, mononuclear cells could be extracted from the patient's blood and induced into macrophages, which are then genetically modified with SIRPα overexpression to create personalized engineered macrophages for further application. Once the patient undergoes surgical resection, the preparation and *in vivo* application of membrane-encapsulated nanoparticles can effectively tackle the challenge of postoperative OS recurrence.

## 4. Materials and methods

### 4.1. Chemicals and reagents

PB was donated by the School of Materials Science and Engineering, Hubei University (Wuhan, China). Information on the fabrication and characterization of the biomaterial has been described previously [49]. Dulbecco's modified Eagle medium (DMEM) and phosphate buffer solution (PBS), 0.25 % trypsin-EDTA solution, dimethyl sulfoxide (DMSO), penicillin–streptomycin (P/S), L-glutamine, sodium pyruvate, and fetal bovine serum (FBS) were all purchased from Gibco Life Technologies Co. (Grand Island, USA). All cell culture and Transwell plates were supplied by Corning (USA). The CCK8 assay kit was purchased from DOJINDO (Japan). Calcein-AM propidium iodide (PI) and 4,6-diamidino-2-phenylindole (DAPI) were purchased from Sigma–Aldrich (USA). Fluorescently labeled antibodies for flow cytometry were purchased from BD Pharmingen (USA). The IP assay was obtained from Absin (China). Antibodies for western blotting and immunofluorescence were supplied by Abcam (USA). The BCA Protein Assay Kit was obtained from Thermo Scientific (23,250, China).

### 4.2. Cell culture

All cells were obtained from the Guangdong Provincial People's Hospital. The murine osteosarcoma cell line K7M2-wt and mouse mononuclear macrophage leukemia cell line RAW264.7 were incubated in DMEM supplemented with 1 % P/S (Invitrogen) and 10 % FBS in a humidified atmosphere containing 5 % CO<sub>2</sub> at 37 °C. Bone marrow-derived macrophages (BMDMs) were extracted as previously described [58]. Briefly, the femurs and tibias of adult male BALB/c mice aged 6–8 weeks were obtained, and the bone marrow was flushed into the culture dish using a 1-mL syringe that was filled with RPMI-1640 medium. The bone marrow-containing medium was resuspended, and red blood cells were lysed using the red blood cell lysis buffer. Monocytes were induced to form mature BMDMs, which were seeded on plates in complete media containing M-CSF (20 ng/mL) for 5 d. Resulting cells were collected using a cell scraper for the following experiments.

### 4.3. Construction of gene-modified cell line

A lentivirus overexpressing SIRPα was obtained from OBiO company (China). As illustrated in Figure S13, the construction map of the SIRPα overexpressed plasmid is presented. Lentivirus transfection was performed on RAW264.7 cells, which were seeded in a 12-well plate at  $2 \times 10^5$  cells per well. Cells were then treated with 1.5 mL of fresh medium containing 6 µg/mL polybrene. After 4 h of incubation at 37 °C with 5 % CO<sub>2</sub>, lentivirus at a multiplicity of infection of 50 were added. After 24 h, the culture medium was replaced with fresh complete media supplemented with 3 µg/mL puromycin. Cells were subsequently transferred to a 10-cm culture dish for purification, which lasted for 48 h. The resulting stable gene-modified cell line was expanded and stored for further experiments.

To knockdown CD47 expression, RAW264.7 cells were transfected with small interfering RNA (siRNA) targeting CD47 (siCD47) or a non-targeting control siRNA (siCtrl) using the Lipofectamine RNAiMAX reagent (Invitrogen) according to the manufacturer's instructions. The siCD47 sequence was designed and synthesized by Ribobio company. The transfection mixture was added to the cells at a final concentration of 20 nM siRNA. After 48 h, cells were harvested for further analysis. CD47 knockdown efficiency was verified by real-time quantitative PCR (RT-qPCR) and Western blot analysis.

### 4.4. Preparation of macrophage cell membranes

SIRPα-overexpressing RAW264.7 cells were stimulated with 1 µg/mL

of lipopolysaccharide (LPS) and incubated at 37 °C with 5 % CO<sub>2</sub> for 24 h. Following incubation, cells were gently scraped from the dish using a clean cell scraper. The cell suspension was then transferred to a sterile 15-mL centrifuge tube, and 50 µL of PMSF ( $100 \times$ ) was added. The cell suspension was rapidly frozen by being placed in liquid nitrogen and then thawed in a 37 °C water bath. This freeze–thaw process was repeated three times to completely disrupt cells. After disruption, the cell suspension was centrifuged at 4 °C, 500 g for 10 min, and then further centrifuged at 4 °C, 10,000 g for 10 min, using a high-speed centrifuge. The supernatant was carefully transferred to an ultracentrifuge tube and centrifuged at 4 °C, 100,000 g for 60 min. This final step isolated cell membrane fragments that were stored at –80 °C. The membrane protein content was assessed using a BCA assay.

### 4.5. Preparation of membrane-coating nanoPB

The nanoPB was dispersed in PBS to 1 mg/mL and subjected to extrusion through a 400-nm membrane using a mini extruder (Avanti) for 20 cycles. The ratio of membrane protein to NP weight was maintained at 1:1. The mixture was then centrifuged at 10,000 rpm for 5 min to remove excess membranes, and then stored at 4 °C. The resulting product was designated as SIRPα-M@nanoPB, while the membranes extruded alone were referred to as SIRPα-M NPs.

### 4.6. Characterization of SIRPα-M@nanoPB

The diameter and the stability of SIRPα-M@nanoPB were measured using a Malvern Zetasizer (Malvern Instruments, UK). A Fourier-transform infrared (FTIR) spectrophotometer (GangDong Technologies, China) was harnessed to observe nanoparticles' FTIR spectra. The morphology was imaged directly using a transmission electron microscope (JEM-1400, Hitachi, Japan). To evaluate the MW thermal effect, nanoPB and SIRPα-M@nanoPB were suspended in saline solution at 1 mg/mL and subjected to MW irradiation of 10 W/cm. The temperature was recorded every 30 s using a FLIR E50 (FLIR Systems Inc, USA).

### 4.7. RT-qPCR

Total RNA was extracted from cells using a Total RNA kit (Omega Bio-tek, USA), and reverse transcription to cDNA was performed using a cDNA synthesis kit (TransGen Biotech, China) on an ABI Veriti PCR (Applied Biosystems, USA). The qPCR for each gene was performed in triplicate using the SYBR green qPCR kit (TransGen Biotech, China) on an ABI 7900 thermocycler (Applied Biosystems, USA) according to the manufacturer's instructions. Specific primer sequences are listed in Table S1. Reactions without any template served as negative controls. Relative mRNA expression was calculated using the  $2^{-\Delta\Delta C_t}$  method.

### 4.8. Coomassie brilliant blue staining

Coomassie brilliant blue staining was conducted following the standard protocol. Briefly, after protein extraction and electrophoresis on a PAGE gel, the gel was submerged in a Coomassie brilliant blue staining solution and gently agitated at room temperature for approximately 2 h, or until faintly visible gel bands were obtained. The gel was then transferred to a destaining solution and gently agitated at room temperature for 4–24 h to eliminate the blue background. Finally, a gel documentation system was used to capture the gel images for subsequent analysis.

### 4.9. Coimmunoprecipitation assay

SIRPα-M NPs (1 mg/mL) were added to K7M2 wild-type cells on a culture plate to investigate the binding between CD47 and SIRPα. After 4 h of coculture, cells were collected using a scraper and lysed with the IP lysis buffer (Thermo Scientific) containing an EDTA-free protease

inhibitor cocktail. Lysates were then incubated on ice for 30 min, followed by centrifugation at 12,000 g for 10 min at 4 °C to obtain the protein supernatants. Samples were divided into three parts and incubated overnight with IgG, anti-CD47, and anti-SIRP $\alpha$  antibodies, respectively. Subsequently, supernatants were subjected to immunoprecipitation using protein A/G beads (Absin) overnight. Beads were washed three times with wash buffer using a magnetic stand. The protein loading buffer was boiled at 100 °C for 5 min, and the mixture was then centrifuged at 14,000 g. The upper liquid was transferred into new tubes for western blotting.

#### 4.10. Western blot analysis

Protein extraction from cells was performed using a protein extraction kit (BB-3101-100T, Best Bio, UK). Protein concentrations were determined using the BCA Protein Assay Kit. Supernatant samples containing 30  $\mu$ g of total protein were collected and heated at 100 °C for 10 min. These samples were then separated by SDS-PAGE and transferred onto 0.22  $\mu$ m polyvinylidene fluoride membranes (ISEQ00010, Merck Millipore, Germany). Membranes were incubated with primary antibodies overnight at 4 °C, according to the manufacturer's recommendations. After three washes in Tris-buffered saline containing 0.1 % Tween-20 (1247ML100, Biofroxx, Germany), membranes were incubated with the appropriate secondary antibodies, including anti-mouse IgG (1:3000, 7076S, Cell Signaling Technology, USA) or anti-rabbit IgG (1:3000, 7074S, Cell Signaling Technology), for 1 h at room temperature. Protein bands were visualized using a chemiluminescence kit (WBKLS0500, Millipore, USA) and detected using the ImageQuant LAS 500 Imager (GE Healthcare Bio-Sciences AB, USA). The optical density of each protein band was quantified using Image J software ( $n = 3$  per group).

#### 4.11. In vitro ROS generation

The Reactive Oxygen Species Assay Kit (Beyotime) was used for the detection of reactive oxygen species. K7M2 cells were seeded at  $1 \times 10^6$  cells/well in six-well plates for 24 h. The control group received 0.9 % NaCl solution, while the nanoPB and the SIRP $\alpha$ -M@nanoPB groups were treated with the corresponding nanoparticles (1 mg/mL). For the MW + groups, a 10-W irradiation microwave probe was used and test sample wells were irradiated for 10 min. After culturing for 24 h, cells were stained according to the manufacturer's protocol and observed using a Nikon 80i microscope (Nikon, Japan).

#### 4.12. Different macrophages-mediated killing and phagocytosis of tumor cells

BMDMs-mediated: K7M2 cells were stained with 10  $\mu$ M of DiO green-fluorescent probe to label their cell membranes, while mature BMDMs were stained with 5  $\mu$ M of Dil red-fluorescent probe for the same purpose. The fluorescently labeled cells were then cocultured on a plate and either treated with or without SIRP $\alpha$ -M@nanoPB. To observe their behaviour, live-cell imaging was performed using a fluorescence microscope in a heated incubation system. Additionally, flow cytometry was used to detect the fluorescence expression after 24 h.

RAW264.7-mediated: the tumour cells utilised in the flow cytometry analysis depicted in Fig. 4C are K7M2 cells, which are equipped with green fluorescent protein (GFP) tags that facilitate excitation in the FITC channel. Raw264.7 cells were utilised with CD45 dye to excite fluorescence in PE channels. Following different of treatments, the cells were collected and examined by flow cytometry.

#### 4.13. In vivo MW thermal activity

All animal procedures were conducted strictly following the guidelines and principles approved by the Ethics Committee of Guangdong

Province's General Hospital (the ethical approval number for animal experimentation: KY-D-2021-402-01). Male BALB/c mice aged 3–4 weeks were obtained from Guangdong Sijiajingda Animal Experiment Co. Ltd. A subcutaneous injection of 100  $\mu$ L of PBS, nanoPB, or SIRP $\alpha$ -M@nanoPB (1 mg/mL) was administered to the left thigh of the mice. Mice were then treated with MW irradiation (10 W, 50 % duty cycle, 5 cm distance), and the temperature of the irradiated surface was monitored.

#### 4.14. In vivo antitumor effects

After 2 weeks of subcutaneous transplantation with K7M2 wt cell suspension, the average tumor volume reached approximately 100 mm<sup>3</sup>, the K7M2-bearing mouse was euthanized, and the tumors were isolated and cut into uniform plaques. After exposing the lateral femoral condyle, the periosteum was removed, and a hole 1–1.5 mm in diameter and 2–2.5 mm in depth was drilled. The tumor mass was embedded into the bone defect. We constructed two types of animal models to evaluate the therapy for primary OS and residual OS tumor.

For the primary model, treatment was performed after 2 weeks, when a significant OS tumor was recognized, and the tumor-bearing mice were randomly divided into six groups: 1) PBS group; 2) nanoPB group; 3) SIRP $\alpha$ -M@nanoPB group; 4) PBS + MW group; 5) nanoPB + MW group; and 6) SIRP $\alpha$ -M@nanoPB + MW group. For the treatment, 100  $\mu$ L of PBS, nanoPB, or SIRP $\alpha$ -M@nanoPB (1 mg/mL) were multi-point injected into the surrounding tumor tissue *in situ* and treated with MW irradiation (10 W, 50 % duty cycle, 5-cm distance) for 5 min. Each treatment was conducted every 3–4 days, and the mice body weight and tumor volume were recorded.

For the residual model, the treatment was conducted at the beginning of tumor embedding. All animals were randomly divided into six groups as a primary model. The treatment was performed during the first 3 days, and the tumor volume was recorded for 20 days.

The tumor volume was calculated as follows:  $V = (\text{short diameter}^2 \times \text{long diameter})/2$ . At the end of the experiment, all mice were euthanized to collect bones containing tumors for subsequent analysis. Microcomputed tomography (micro-CT) was employed to assess bone absorption. Histological staining techniques, including H&E staining, Ki67 staining, TUNEL assay, and immunofluorescent experiments, such as the detection of F4/80, CD11b, CD86, and CD206, were implemented to demonstrate tumor proliferation and the modulation of immune cells in the TME.

#### 4.15. In vivo antitumor immunity

After the completion of the treatment of K7M2 tumor-bearing mice, tumors were collected and digested using the Tumor Dissociation Kit from Miltenyi. Flow cytometry analysis was conducted to determine the presence of tumor-infiltrating macrophages and activated T cells. For macrophage polarization evaluation, antibodies against F4/80, CD86, and CD206 were added. Antibodies against DC cells (CD4 and CD8) were added to assess the frequency of CD4<sup>+</sup> and CD8<sup>+</sup> T cells. The process of fixation, permeabilization, and staining followed the manufacturer's protocols. The gating strategy of macrophages: Initially, cells in FSC-A and SSC-A were selected, and subsequently, FSC-A and FSC-H were utilised to eliminate the adhesion. Finally, the F4/80<sup>+</sup> + CD11b<sup>+</sup> + CD86<sup>+</sup> cells were identified as M1-polarized macrophages. Conversely, F4/80<sup>+</sup> + CD11b<sup>+</sup> + CD206<sup>+</sup> cells were identified as M2-polarized macrophages. The gating strategy of T cells: Initially, cells in FSC-A and SSC-A were selected, followed by FSC-A and FSC-H to eliminate adhesion. Subsequently, the CD45<sup>+</sup> marker was utilised to delineate lymphocytes, while the CD3<sup>+</sup> marker was employed to identify T cells. Finally, CD4<sup>+</sup> cells were defined as CD4 T cells, and CD8<sup>+</sup> cells were defined as CD8 T cells.



#### 4.16. Statistical analysis

Data analysis and graphing were performed using GraphPad Prism 9. The comparison between the two groups was conducted using the *t*-test method. Results were presented as mean  $\pm$  standard deviation (Mean  $\pm$  SD). Significance was noted as:  $*p < 0.05$ ,  $**p < 0.01$ ,  $***p < 0.001$ , and  $****p < 0.0001$ . All statistical results in this experiment were based on at least three independent experiments.

#### 5. Conclusion

This study successfully developed a novel nanotherapeutic, SIRP $\alpha$ -M@nanoPB, by encapsulating genetically modified cell membranes onto microwave-responsive nanoPB. The successful encapsulation and retention of the cell membrane were confirmed through western blotting, electron microscopy, and the presence of proteins on the membrane surface. SIRP $\alpha$ -M@nanoPB demonstrated high cell compatibility and repeatable thermal effects, making it a promising candidate for clinical applications. *In vitro* experiments convincingly showed the significant regulatory role of macrophages in enhancing phagocytic and killing activity against tumor cells by disrupting the CD47–SIRP $\alpha$  immune-suppression checkpoint. Furthermore, *in vivo* experiments validated the microwave-heating effect, tumor cell-killing effect, and regulation of TAMs by SIRP $\alpha$ -M@nanoPB. This innovative approach, synergistically combining thermotherapy and immunotherapy, holds considerable potential for safely treating residual OS tumors after surgery in clinical settings. The development of SIRP $\alpha$ -M@nanoPB represents a significant step forward in the field of nanomedicine and cancer therapy, offering a new avenue for targeted and effective OS treatment.

#### CRediT authorship contribution statement

**Xiongfa Ji:** Writing – original draft, Funding acquisition. **Xin Qian:** Software, Methodology. **Guowen Luo:** Visualization, Methodology. **Wenjie Yang:** Formal analysis. **Wenhan Huang:** Writing – review & editing. **Zehua Lei:** Writing – review & editing. **Jiaqi Zhou:** Visualization. **Guoqing Zhong:** Software. **Jielong Zhou:** Data curation. **Nan Liu:** Data curation. **Limin Ma:** Formal analysis. **Mei Li:** Investigation. **Xiangmei Liu:** Resources, Investigation. **Shuilin Wu:** Writing – review & editing, Supervision. **Yu Zhang:** Supervision, Project administration.

#### Declaration of competing interest

Shuilin Wu is an editorial board member for Bioactive Materials and was not involved in the editorial review or the decision to publish this article. All authors declare that there are no competing interests.

#### Ethics approval and consent to participate

All animal procedures were conducted strictly following the guidelines and principles approved by the Ethics Committee of Guangdong Province's General Hospital (the ethical approval number for animal experimentation: KY-D-2021-402-01).

#### Acknowledgements

X.J., X.Q. and G.L. contributed equally to this work.

This work was supported by the grants from Key project of Regional Innovation Joint Fund of National Natural Science Foundation of China (U21A2084) and National Key Research and Development Project (2021YFC2400704), the National Natural Science Foundation of China (Grant No. 52271244, 32471421, 32101097), the Natural Science Foundation of Guangdong Province, China (Grant No. 2022A1515010202, 2023A1515011544).

#### Appendix A. Supplementary data

Supplementary data to this article can be found online at <https://doi.org/10.1016/j.bioactmat.2025.01.012>.

#### References

- [1] Nat. Rev. Dis. Prim. 8 (1) (2022) 76.
- [2] A. Jemal, R. Siegel, E. Ward, Y. Hao, J. Xu, T. Murray, M.J. Thun, CA: a cancer journal for clinicians 58 (2) (2008) 71–96.
- [3] G.A. Odri, J. Tchicaya-Bouanga, D.J.Y. Yoon, D. Modrowski, Cancers 14 (2) (2022) 360.
- [4] G. Sheng, Y. Gao, Y. Yang, H. Wu, Front. Oncol. 11 (2021) 780264.
- [5] C.A. Klein, Nat. Rev. Cancer 20 (11) (2020) 681–694.
- [6] V. Mialou, T. Philip, C. Kalifa, D. Perol, J.C. Gentet, P. Marec-Berard, H. Pacquement, P. Chastagner, A.S. Defaschelles, O. Hartmann, Cancer 104 (5) (2005) 1100–1109.
- [7] R. Baghban, L. Roshangar, R. Jahanban-Esfahlan, K. Seidi, A. Ebrahimi-Kalan, M. Jaymand, S. Kolahian, T. Javaheri, P. Zare, Cell Commun. Signal. 18 (1) (2020) 59.
- [8] A.E. Bădilă, D.M. Rădulescu, A.-G. Niculescu, A.M. Grumezescu, M. Rădulescu, A. R. Rădulescu, Cancers 13 (16) (2021) 4229.
- [9] J. Martín-Broto, D.S. Moura, B.A. Van Tine, Clin. Cancer Res. 26 (22) (2020) 5801–5808.
- [10] K.F. Chu, D.E. Dupuy, Nat. Rev. Cancer 14 (3) (2014) 199–208.
- [11] T.T. Healey, B.T. March, G. Baird, D.E. Dupuy, J. Vasc. Intervent. Radiol. 28 (2) (2017) 206–211.
- [12] K. Leuchte, E. Staib, M. Thelen, P. Gödel, A. Lechner, P. Zentis, M. Garcia-Marquez, D. Waldschmidt, R.R. Datta, R. Wahba, C. Wybranski, T. Zander, A. Quaa, U. Drebbler, D.L. Stippel, C. Bruns, M. von Bergwelt-Baildon, K. Wennhold, H. A. Schlößer, Cancer Immunol. Immunother. 70 (4) (2021) 893–907.
- [13] A.F. Kamal, H. Widyawarman, K. Husodo, E.U. Hutagalung, W. Rajabto, Acta Med. Indones. 48 (3) (2016) 175–183.
- [14] G. Carratello, D. Laganà, M. Mangini, F. Fontana, G. Dionigi, L. Boni, F. Rovera, S. Cuffari, C. Fugazzola, Int. J. Surg. 6 (Suppl 1) (2008) S65–S69.
- [15] Q.Y. Fan, Y. Zhou, M. Zhang, B. Ma, T. Yang, H. Long, Z. Yu, Z. Li, Front Surg 6 (2019) 5.
- [16] K. Zheng, X. Yu, Y. Hu, Y. Zhang, Z. Wang, S. Wu, J. Shen, Z. Ye, C. Tu, Y. Zhang, X. Wei, Y. Hu, X. Wang, J. Li, H. Duan, Y. Wu, M. Xu, Z. Yuan, Y. Wei, B. Chen, Orthop. Surg. 12 (4) (2020) 1036–1044.
- [17] C. Fu, H. Zhou, L. Tan, Z. Huang, Q. Wu, X. Ren, J. Ren, X. Meng, ACS Nano 12 (3) (2018) 2201–2210.
- [18] S. Li, Z. Chen, L. Tan, Q. Wu, X. Ren, C. Fu, M. Niu, H. Li, X. Meng, Biomaterials 283 (2022) 121472.
- [19] N.A. Giraldo, R. Sanchez-Salas, J.D. Peske, Y. Vano, E. Becht, F. Petitprez, P. Validire, A. Ingels, X. Cathelineau, W.H. Fridman, C. Sautès-Fridman, Br. J. Cancer 120 (1) (2019) 45–53.
- [20] Q. Huang, X. Liang, T. Ren, Y. Huang, H. Zhang, Y. Yu, C. Chen, W. Wang, J. Niu, J. Lou, W. Guo, Cell. Oncol. 44 (3) (2021) 525–539.
- [21] K.E. de Visser, J.A. Joyce, Cancer Cell 41 (3) (2023) 374–403.
- [22] S. Chen, A.F.U.H. Saeed, Q. Liu, Q. Jiang, H. Xu, G.G. Xiao, L. Rao, Y. Duo, Signal Transduct. Targeted Ther. 8 (1) (2023) 207.
- [23] S.B. Willingham, J.-P. Volkmer, A.J. Gentles, D. Sahoo, P. Dalerba, S.S. Mitra, J. Wang, H. Contreras-Trujillo, R. Martin, J.D. Cohen, P. Lovelace, F.A. Scheeren, M.P. Chao, K. Weiskopf, C. Tang, A.K. Volkmer, T.J. Naik, T.A. Storm, A.R. Mosley, B. Edris, S.M. Schmid, C.K. Sun, M.-S. Chua, O. Murillo, P. Rajendran, A.C. Cha, R. K. Chin, D. Kim, M. Adorno, T. Raveh, D. Tseng, S. Jaiswal, P.Ø. Enger, G. K. Steinberg, G. Li, S.K. So, R. Majeti, G.R. Harsh, M. van de Rijn, N.N.H. Teng, J. B. Sunwoo, A.A. Alizadeh, M.F. Clarke, I.L. Weissman, Proc. Natl. Acad. Sci. USA 109 (17) (2012) 6662–6667.
- [24] Z. Wang, B. Li, S. Li, W. Lin, Z. Wang, S. Wang, W. Chen, W. Shi, T. Chen, H. Zhou, E. Yinwang, W. Zhang, H. Mou, X. Chai, J. Zhang, Z. Lu, Z. Ye, Nat. Commun. 13 (1) (2022) 6308.
- [25] C. Huang, X. Wang, Y. Wang, Y. Feng, X. Wang, S. Chen, P. Yan, J. Liao, Q. Zhang, C. Mao, Y. Li, L. Wang, X. Wang, W. Yi, W. Cai, S. Chen, N. Hong, W. He, J. Chen, W. Jin, Nat. Cancer 5 (3) (2024) 500–516.
- [26] Y.e. Liu, Y. Wang, Y. Yang, L. Weng, Q. Wu, J. Zhang, P. Zhao, L. Fang, Y. Shi, P. Wang, Signal Transduct. Targeted Ther. 8 (1) (2023) 104.
- [27] S. Sheng, L. Jin, Y. Zhang, W. Sun, L. Mei, D. Zhu, X. Dong, F. Lv, ACS Nano 18 (6) (2024) 4981–4992.
- [28] H. Al-Sudani, Y. Ni, P. Jones, H. Karakilic, L. Cui, L.D.S. Johnson, P.G. Rose, A. Olawaiye, R.P. Edwards, R.A. Uger, G.H.Y. Lin, H. Mahdi, npj Precis. Oncol. 7 (1) (2023) 69.
- [29] X. Huang, L. Wang, H. Guo, W. Zhang, Bioact. Mater. 23 (2023) 69–79.
- [30] N. Krishnan, R.H. Fang, L. Zhang, Clin. Transl. Med. 13 (6) (2023) e1285.
- [31] Y. Zeng, S. Li, S. Zhang, L. Wang, H. Yuan, F. Hu, Acta Pharm. Sin. B 12 (8) (2022) 3233–3254.
- [32] R.H. Fang, W. Gao, L. Zhang, Nat. Rev. Clin. Oncol. 20 (1) (2023) 33–48.
- [33] Y. Lin, J.L. Zhao, Q.J. Zheng, X. Jiang, J. Tian, S.Q. Liang, H.W. Guo, H.Y. Qin, Y. M. Liang, H. Han, Front. Immunol. 9 (2018) 1744.
- [34] S. Wei, Y. Qiao, Z. Wu, X. Liu, Y. Li, Z. Cui, C. Li, Y. Zheng, Y. Liang, Z. Li, S. Zhu, H. Wang, X. Wang, R. Che, S. Wu, Nano Today 37 (2021) 101090.
- [35] K.R. Neupane, J.R. McCorkle, T.J. Kopper, J.E. Lakes, S.P. Aryal, M. Abdullah, A. A. Snell, J.C. Gensel, J. Kolesar, C.I. Richards, ACS Omega 6 (5) (2021) 3847–3857.
- [36] J. Dong, X. Chai, Y. Xue, S. Shen, Z. Chen, Z. Wang, E. Yinwang, S. Wang, L. Chen, F. Wu, H. Li, Z. Chen, J. Xu, Z. Ye, X. Li, Q. Lu, Small 20 (29) (2024) e2309038.
- [37] Y. Zhou, Y. Yao, Y. Deng, A. Shao, Cell Commun. Signal. 18 (1) (2020) 71.
- [38] J.E. Bader, K. Voss, J.C. Rathmell, Mol. Cell 78 (6) (2020) 1019–1033.

- [39] L.K. Chim, I.L. Williams, C.J. Bashor, A.G. Mikos, *Biomaterials* 296 (2023) 122076.
- [40] J. Muñoz-García, D. Cochonneau, S. Télétchéa, E. Moranton, D. Lanoe, R. Brion, F. Lézot, M.-F. Heymann, D. Heymann, *Theranostics* 11 (4) (2021) 1568–1593.
- [41] G.S. Lubitz, J.D. Brody, *Nat. Rev. Immunol.* 22 (1) (2022) 3, 3.
- [42] Z.-H. Ye, W.-B. Yu, M.-Y. Huang, J. Chen, J.-J. Lu, *Acta Pharm. Sin. B* 13 (4) (2023) 1467–1487.
- [43] L. Tang, Y. Yin, Y. Cao, C. Fu, H. Liu, J. Feng, W. Wang, X.J. Liang, *Adv Mater* 35 (35) (2023) e2303835.
- [44] J. Zhu, C. Cai, J. Li, J. Xiao, X. Duan, *Medicine in Drug Discovery* 15 (2022) 100139.
- [45] Z. Bian, L. Shi, K. Kidder, K. Zen, C. Garnett-Benson, Y. Liu, *Nat. Commun.* 12 (1) (2021) 3229.
- [46] F. Martins, L. Sofiya, G.P. Sykietis, F. Lamine, M. Maillard, M. Fraga, K. Shabafrouz, C. Ribí, A. Cairolí, Y. Guex-Crosier, T. Kuntzer, O. Michielin, S. Peters, G. Coukos, F. Spertini, J.A. Thompson, M. Obeid, *Nat. Rev. Clin. Oncol.* 16 (9) (2019) 563–580.
- [47] X. Deng, Z. Shao, Y. Zhao, *Adv. Sci.* 8 (3) (2021) 2002504.
- [48] X. Liang, G. Wang, W. Gu, G. Ji, *Carbon* 177 (2021) 97–106.
- [49] J. Li, X. Liu, L. Tan, Z. Cui, X. Yang, Y. Liang, Z. Li, S. Zhu, Y. Zheng, K.W.K. Yeung, X. Wang, S. Wu, *Nat. Commun.* 10 (1) (2019) 4490.
- [50] H. Liu, Y.-Y. Su, X.-C. Jiang, J.-Q. Gao, *Drug Delivery and Translational Research* 13 (3) (2023) 716–737.
- [51] B. Li, W. Wang, L. Zhao, Y. Wu, X. Li, D. Yan, Q. Gao, Y. Yan, J. Zhang, Y. Feng, J. Zheng, B. Shu, J. Wang, H. Wang, L. He, Y. Zhang, M. Pan, D. Wang, B.Z. Tang, Y. Liao, *Nat. Nanotechnol.* (2024).
- [52] D. Wu, X. Shou, Y. Zhang, Z. Li, G. Wu, D. Wu, J. Wu, S. Shi, S. Wang, *Nanomedicine* 32 (2021) 102333.
- [53] S. Barua, S. Mitragotri, *Nano Today* 9 (2) (2014) 223–243.
- [54] J. Lopes, D. Lopes, M. Pereira-Silva, D. Peixoto, F. Veiga, M.R. Hamblin, J. Conde, C. Corbo, E.N. Zare, M. Ashrafizadeh, F.R. Tay, C. Chen, R.F. Donnelly, X. Wang, P. Makvandi, A.C. Paiva-Santos, *Small Methods* 6 (8) (2022) 2200289.
- [55] C. Yau, M. Osdoit, M. van der Noordaa, S. Shad, J. Wei, D. de Croze, A.-S. Hamy, M. Laé, F. Reyat, G.S. Sonke, T.G. Steenbruggen, M. van Seijen, J. Wesseling, M. Martín, M. del Monte-Millán, S. López-Tarruella, K. Adamson, K.S. Albain, A. L. Asare, S.M. Asare, R. Balassanian, H. Beckwith, S.M. Berry, D.A. Berry, J. C. Boughey, M.B. Buxton, Y.-Y. Chen, B. Chen, A.J. Chien, S.Y. Chui, A.S. Clark, J. L. Clennell, B. Datnow, A.M. DeMichele, X. Duan, K.K. Edmiston, A.D. Elias, E. D. Ellis, L.L. Esserman, D.M. Euhus, O. Fadare, F. Fan, M.D. Feldman, A. Forero-Torres, B.B. Haley, H.S. Han, S. Harada, P. Haugen, T. Helsten, G.L. Hirst, N. M. Hylton, C. Isaacs, K. Kemmer, Q.J. Khan, L. Khazai, M.E. Klein, G. Krings, J. E. Lang, L.G. LeBeau, B. Leyland-Jones, M.C. Liu, S. Lo, J. Lu, A. Magliocco, J. B. Matthews, M.E. Melisko, P. Mhawech-Fauceglia, S.L. Moulder, R.K. Murthy, R. Nanda, D.W. Northfelt, I.T. Ocal, O. Olopade, S. Pambuccian, M. Paoloni, J. W. Park, B.A. Parker, J. Perlmutter, G. Peterson, L. Pusztai, M. Rendí, H.S. Rugo, S. Sahoo, S. Sams, A. Sanil, H. Sattar, R.B. Schwab, R. Singhrao, K. Steeg, E. Stringer-Reasor, W.F. Symmans, O. Tawfik, D. Tripathy, M.L. Troxell, L.J. van't Veer, S.J. Venters, T. Vinh, R.K. Viscusi, A.M. Wallace, S. Wei, A. Wilson, C. Yau, D. Yee, J.C. Zeck, J.C. Boughey, M.P. Goetz, T. Hoskin, R. Gould, V. Valero, S. B. Edge, J.E. Abraham, J.M.S. Bartlett, C. Caldas, J. Dunn, H. Earl, L. Hayward, L. Hiller, E. Provenzano, S.-J. Sammut, J.S. Thomas, D. Cameron, A. Graham, P. Hall, L. Mackintosh, F. Fan, A.K. Godwin, K. Schwensen, P. Sharma, A. M. DeMichele, K. Cole, L. Pusztai, M.-O. Kim, L.J. van 't Veer, L.J. Esserman, W. F. Symmans, *Lancet Oncol.* 23 (1) (2022) 149–160.
- [56] A. Tiwari, *J Clin Orthop Trauma* 3 (1) (2012) 4–9.
- [57] J.E. Talmadge, I.J. Fidler, *Cancer Res.* 70 (14) (2010) 5649–5669.
- [58] X. Ji, H. Shao, X. Li, M.W. Ullah, G. Luo, Z. Xu, L. Ma, X. He, Z. Lei, Q. Li, X. Jiang, G. Yang, Y. Zhang, *Biomaterials, Materials & Correspondence* 285 (2022) 121530.